

Electronic, Magnetic, and Redox Properties and O₂ Reactivity of Iron(II) and Nickel(II) *o*-Semiquinonate Complexes of a Tris(thioether) Ligand: Uncovering the Intradiol Cleaving Reactivity of an Iron(II) *o*-Semiquinonate Complex

Peng Wang,[†] Michelle M. Killian,[‡] Mohamed R. Saber,[§] Tian Qiu,[†] Glenn P. A. Yap,[†] Codrina V. Popescu,^{||} Joel Rosenthal,[†] Kim R. Dunbar,[§] Thomas C. Brunold,[‡] and Charles G. Riordan^{*,†}

[†]Department of Chemistry and Biochemistry, University of Delaware, Newark, Delaware 19716, United States

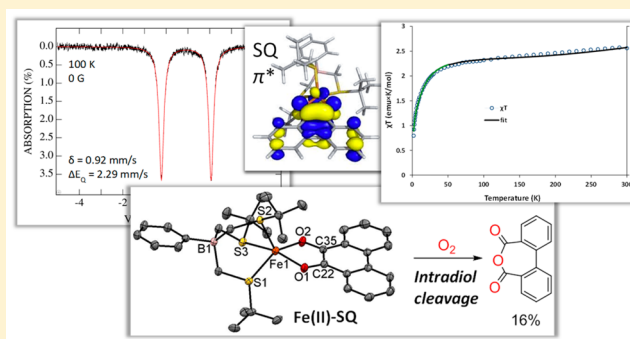
[‡]Department of Chemistry, University of Wisconsin—Madison, Madison, Wisconsin 53706, United States

[§]Department of Chemistry, Texas A&M University, College Station, Texas 77842-3012, United States

^{||}Department of Chemistry, Colgate University, 13 Oak Drive, Hamilton, New York 13346, United States

Supporting Information

ABSTRACT: The iron(II) semiquinonate character within the iron(III) catecholates species has been proposed by numerous studies to account for the O₂ reactivity of intradiol catechol dioxygenases, but a well-characterized iron(II) semiquinonate species that exhibits intradiol cleaving reactivity has not yet been reported. In this study, a detailed electronic structure description of the first iron(II) *o*-semiquinonate complex, [PhTt^{tBu}Fe(phenSQ)] [PhTt^{tBu} = phenyltris(*tert*-butylthiomethyl)borate; phenSQ = 9,10-phenanthrenesemiquinonate; Wang et al. *Chem. Commun.* **2014**, *50*, 5871–5873], was generated through a combination of electronic and Mössbauer spectroscopies, SQUID magnetometry, and density functional theory (DFT) calculations. [PhTt^{tBu}Fe(phenSQ)] reacts with O₂ to generate an intradiol cleavage product, diphenic anhydride, in 16% yield. To assess the dependence of the intradiol reactivity on the identity of the metal ion, the nickel analogue, [PhTt^{tBu}Ni(phenSQ)], and its derivative, [PhTt^{tBu}Ni(3,5-DBSQ)] (3,5-DBSQ = 3,5-di-*tert*-butyl-1,2-semiquinonate), were prepared and characterized by X-ray crystallography, mass spectrometry, ¹H NMR and electronic spectroscopies, and SQUID magnetometry. DFT calculations, evaluated on the basis of the experimental data, support the electronic structure descriptions of [PhTt^{tBu}Ni(phenSQ)] and [PhTt^{tBu}Ni(3,5-DBSQ)] as high-spin nickel(II) complexes with antiferromagnetically coupled semiquinonate ligands. Unlike its iron counterpart, [PhTt^{tBu}Ni(phenSQ)] decomposes slowly in an O₂ atmosphere to generate 14% phenanthrenequinone with a negligible amount of diphenic anhydride. [PhTt^{tBu}Ni(3,5-DBSQ)] does not react with O₂. This dramatic effect of the metal-ion identity supports the hypothesis that a metal(III) alkylperoxo species serves as an intermediate in the intradiol cleaving reactions. The redox properties of all three complexes were probed using cyclic voltammetry and differential pulse voltammetry, which indicate an inner-sphere electron-transfer mechanism for the formation of phenanthrenequinone. The lack of O₂ reactivity of [PhTt^{tBu}Ni(3,5-DBSQ)] can be rationalized by the high redox potential of the metal-ligated 3,5-DBSQ/3,5-DBQ couple.



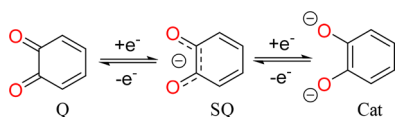
1. INTRODUCTION

Transition-metal dioxolene complexes continue to attract much interest, in part because of their applications as redox-active ligands and their relevance to catechol dioxygenase enzymes.^{1–3} As a well-established redox-active ligand, dioxolene can exist in three different oxidation states: neutral (quinone), monoanionic (semiquinonate), and dianionic (catecholate) (Scheme 1). All three redox forms have been explored in transition-metal dioxolene chemistry, which led to various intriguing observations such as valence tautomerization,^{4–7} spin-crossover,^{8–14} biomimetic properties,^{15–18} and catalytic activities.^{19–24}

Our interest in transition-metal dioxolene complexes stems from their biological significance. An iron(III) catecholate species was identified in the active sites of intradiol catechol dioxygenases, enzymes that catalyze the oxidative cleavage of the C1–C2 bond of catechols.^{16,25} The form of the enzyme that react with O₂ contains a five-coordinate iron(III) site. One of the proposed mechanisms for how the iron(III) catecholate species activates O₂ invokes the mixing of an iron(II)

Received: June 12, 2017

Scheme 1. Redox Series of Quinone (Q)–Semiquinonate (SQ)–Catecholate (Cat)



semiquinonate state into the iron(III) catecholate ground state. According to this mechanism (Scheme 2), iron(II) *o*-semiquinonate is the “active form” that reacts with O₂ to generate an iron(III) alkylperoxy intermediate²⁶ with a monodentate dioxolene moiety. The iron(III) alkylperoxy intermediate then undergoes a Criegee rearrangement, followed by ring opening to subsequently yield the intradiol cleavage product. This proposal has been supported by theoretical calculations^{27–30} and the observed correlations between the spectroscopic features and intradiol reactivity of iron(III) catecholate model compounds.^{31–35} Nevertheless, to the best of our knowledge, direct observation of the intradiol cleaving reactivity of a well-defined iron(II) semiquinonate species had not previously been reported.

In a recent communication, some of us reported the preparation and characterization of the first mononuclear iron(II) *o*-semiquinonate complex, namely, [PhTt^{tBu}]₂Fe(phenSQ)³⁶ (Figure 1). On the basis of the average C–O distance of the dioxolene ligand, 1.285(2) Å, the redox state of the dioxolene ligand was assigned as a semiquinonate. Furthermore, the existence of a five-coordinate high-spin iron(II) ion was inferred on the basis of the ligand-field (LF) transition at 935 nm (539 M⁻¹ cm⁻¹; Figure 1). Given the scarcity of mononuclear iron(II) *o*-semiquinonate species and their proposed involvement in the mechanism of O₂ activation by intradiol catechol dioxygenases and their model compounds, it is highly desirable to gain insight into the electronic structure of [PhTt^{tBu}]₂Fe(phenSQ) and to examine its reactivity with O₂.

Herein, we report spectroscopic and magnetic studies in conjunction with density functional theory (DFT) calculations to further interrogate the electronic structure of [PhTt^{tBu}]₂Fe-

(phenSQ). In addition, studies of the O₂ reactivity of [PhTt^{tBu}]₂Fe(phenSQ) led to the discovery of the first synthetic iron(II) *o*-semiquinonate species exhibiting intradiol cleaving reactivity. For comparison to [PhTt^{tBu}]₂Fe(phenSQ), two nickel *o*-semiquinonate analogues were prepared, namely, [PhTt^{tBu}]₂Ni(phenSQ) and [PhTt^{tBu}]₂Ni(3,5-DBSQ). The solid-state structures, electronic and magnetic properties, and redox behaviors of these new nickel complexes are presented and discussed. Finally, comparative O₂ reactivity studies of the iron(II) and nickel(II) *o*-semiquinonate complexes highlight the fundamental effect of the metal ion on the intradiol cleaving reactivity.

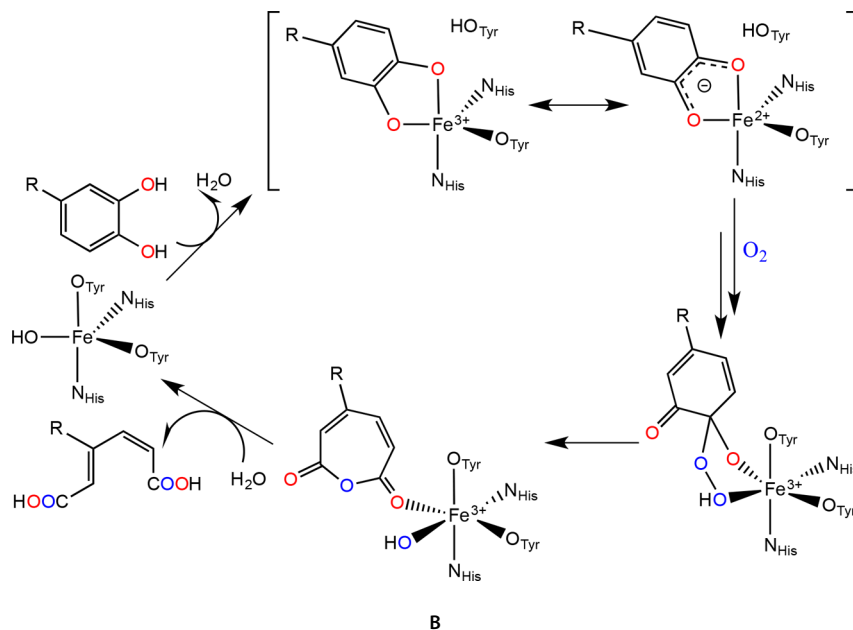
2. EXPERIMENTAL AND COMPUTATIONAL METHODS

2.1. General Information. All air- and moisture-sensitive reactions were performed under N₂ using standard Schlenk techniques or carried out under an Ar or N₂ atmosphere in a Vacuum Atmospheres glovebox equipped with a gas purification system. Unless otherwise noted, all reagents were purchased from commercial sources and used without further purification. Anhydrous NiI₂ was purchased from Strem Chemicals. Solvents were of reagent-grade or better and were dried by passage through activated alumina and then stored over 4 Å molecular sieves prior to use. Deuterated solvents were purchased from Cambridge Isotope Laboratories and stored over 4 Å molecular sieves. [PhTt^{tBu}]₂Ti,³⁷ Ti(phenSQ),³⁸ and Ti(3,5-DBSQ)³⁸ were prepared following published procedures.

2.2. Synthesis. **2.2.1. [PhTt^{tBu}]₂NiI.** Anhydrous NiI₂ (1.250 g, 4.0 mmol) was ground into a fine powder and suspended in 100 mL of tetrahydrofuran (THF). After stirring for 6 h, [PhTt^{tBu}]₂TiI (1.204 g, 2.0 mmol) was added in small portions. After stirring for 16 h, the reaction mixture was filtered through Celite, removing TiI, and the solvent was removed in vacuo. The residue was extracted with pentane (2 × 40 mL), and the resulting red solution was filtered through Celite. Removal of the solvent under reduced pressure afforded a brown solid (919 mg, 69%). ¹H NMR (C₆D₆): δ 15.2 (27H, br, C(CH₃)₃S), 11.1 (2H, s, *m*-(C₆H₅)B), 8.5 (2H, s, *o*-(C₆H₅)B), 8.3 (1H, s, *p*-(C₆H₅)B). UV–vis [toluene; λ_{max} nm (ε, M⁻¹ cm⁻¹): 311 (1518), 375 (sh), 413 (sh), 452 (6036), 567 (972), 841 (427), 903 (432). Anal. Calcd for C₂₁H₃₈BNiS₃: C, 43.26; H, 6.57. Found: C, 43.50; H, 6.80.

2.2.2. [PhTt^{tBu}]₂Ni(phenSQ). A suspension of Ti(phenSQ) (83 mg, 0.20 mmol) in 30 mL of THF was added dropwise over 20–30 min to

Scheme 2. Proposed Mechanism for Intradiol catechol Dioxygenases Highlighting Iron(II) *o*-Semiquinonate as the Active Form Responsible for O₂ Activation



B

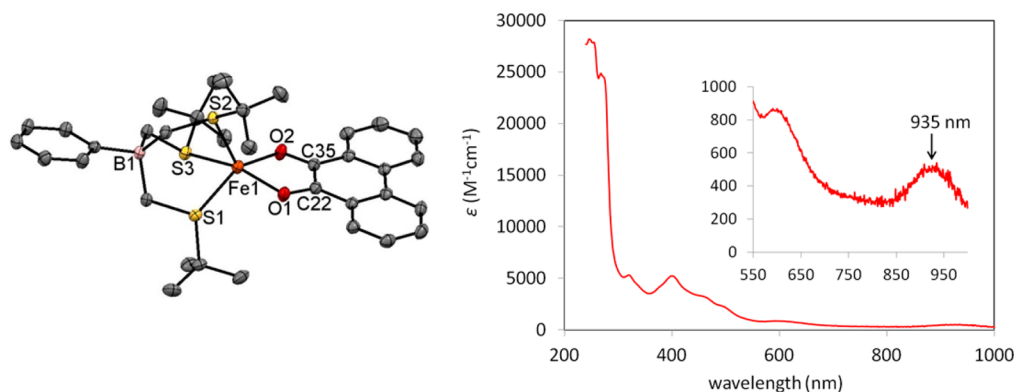


Figure 1. X-ray structure of $[\text{PhTt}^{\text{tBu}}]\text{Fe}(\text{phenSQ})$ (left) and electronic absorption spectrum measured in THF (right).

a stirring solution of $[\text{PhTt}^{\text{tBu}}]\text{NiI}$ (117 mg, 0.20 mmol) in 10 mL of THF. A yellow precipitate gradually formed as the color of the solution turned from orange-red to purple. The mixture was stirred for 6 h and then filtered through a pad of Celite. THF was removed in vacuo, and the residue was washed with pentane (2×4 mL) and then extracted with pentane/diethyl ether (1:1, v/v). Filtration of the extract through a Celite pad, followed by solvent removal in vacuo, yielded a dark-purple powder (106 mg, 80%). Slow evaporation of a concentrated pentane/diethyl ether (2:1, v/v) solution of the product yielded crystals suitable for X-ray diffraction (XRD) analysis. $^1\text{H NMR}$ (C_6D_6): δ 52.6 (br), 9.4 (br, $\text{C}(\text{CH}_3)_3\text{S}$), -4.1 (br). UV-vis [toluene; λ_{max} nm (ϵ , $\text{M}^{-1}\text{cm}^{-1}$): 316 (9131), 398 (12877), 536 (11375), 586 (10011), 846 (710), 966 (sh). LIFDI-MS. Calcd for $\text{C}_{35}\text{H}_{46}\text{BNiO}_2\text{S}_3$ [$(\text{M})^+$, 100%]: m/z 663.2113. Found: m/z 663.2093. μ_{eff} (C_6D_6): 2.18(3) μ_{B} . Anal. Calcd for $\text{C}_{35}\text{H}_{46}\text{BNiO}_2\text{S}_3$: C, 63.27; H, 6.98. Found: C, 63.31; H, 7.18.

2.2.3. $[\text{PhTt}^{\text{tBu}}]\text{Ni}(3,5\text{-DBSQ})$. A solution of $\text{Ti}(3,5\text{-DBSQ})$ (178 mg, 0.42 mmol) in 50 mL of THF was added dropwise over 30 min to a stirring solution of $[\text{PhTt}^{\text{tBu}}]\text{NiI}$ (233 mg, 0.40 mmol) in 20 mL of diethyl ether. A yellow precipitate gradually formed as the color of the solution turned from orange-red to red-purple. The mixture was stirred for 6 h and then filtered through a pad of Celite. The solvent was removed in vacuo, and the residue was extracted with pentane. Filtration of the extract through Celite followed by solvent removal in vacuo yielded a dark-brown powder (230 mg, 85%). Slow evaporation of a concentrated pentane solution of the product yielded crystals suitable for XRD analysis. $^1\text{H NMR}$ (C_6D_6): δ 10.3 (sh), 9.2 (br, $\text{C}(\text{CH}_3)_3\text{S}$), -7.1 (br). UV-vis [toluene; λ_{max} nm (ϵ , $\text{M}^{-1}\text{cm}^{-1}$): 300 (7328), 366 (sh), 522 (5811), 566 (sh), 842 (823), 966 (sh). LIFDI-MS. Calcd for $\text{C}_{35}\text{H}_{58}\text{BNiO}_2\text{S}_3$ [$(\text{M})^+$, 100%]: m/z 675.3052. Found: m/z 675.3093. μ_{eff} (C_6D_6): 2.25 μ_{B} .

2.3. Examining the Reaction of $[\text{PhTt}^{\text{tBu}}]\text{Fe}(\text{PhenSQ})$ with O_2 by Liquid-Injection Field Desorption Ionization Mass Spectrometry (LIFDI-MS). In an Ar-filled glovebox, $[\text{PhTt}^{\text{tBu}}]\text{Fe}(\text{PhenSQ})$ (3.0 mg, 0.0045 mmol) was dissolved in 10 mL of toluene, and 4 mL of the solution was transferred to a 20 mL scintillation vial charged with a magnetic stir bar. The vial was then sealed with a rubber septum and removed from the glovebox. The solution was degassed by two freeze-pump-thaw cycles, and the vial was then immersed in a dry ice/acetone bath (-78 °C). With stirring, the solution was exposed to 1 atm of dry O_2 at -78 °C. After 5 min, the solution was warmed to room temperature and the LIFDI-MS spectrum was taken.

2.4. Examining the Reaction of $[\text{PhTt}^{\text{tBu}}]\text{Fe}(\text{PhenSQ})$ with O_2 by $^1\text{H NMR}$ Spectroscopy and Gas Chromatography (GC). In an Ar-filled glovebox, $[\text{PhTt}^{\text{tBu}}]\text{Fe}(\text{PhenSQ})$ (30 mg, 0.045 mmol) was dissolved in 10 mL of toluene in a 100 mL Schlenk flask charged with a magnetic stir bar. The solution was removed from the glovebox and degassed by two freeze-pump-thaw cycles. The flask was then immersed in a dry ice/acetone bath (-78 °C), and 1 atm of dry O_2 was added through a needle. The solution was stirred at -78 °C for 30 min, then warmed to room temperature, and stirred for an additional 30 min (the pressure of O_2 was released via an outlet needle as the

sample warmed). The solution was concentrated to 2–3 mL in vacuo, and 0.5 M HCl (2 mL, 0.5 mmol) was added to dissociate the metal from the organic products. After the mixture was stirred for 5 min, 15 mL of H_2O was added, and the sample was extracted with ethyl acetate (3×20 mL). The organic extracts were combined and dried over anhydrous Na_2SO_4 . After removal of ethyl acetate in vacuo, the products were obtained and analyzed by $^1\text{H NMR}$ spectroscopy (CDCl_3) and GC.

2.5. Examining the Reaction of $[\text{PhTt}^{\text{tBu}}]\text{Ni}(\text{PhenSQ})$ with O_2 by Electronic Absorption Spectroscopy, $^1\text{H NMR}$ Spectroscopy, and GC. $[\text{PhTt}^{\text{tBu}}]\text{Ni}(\text{PhenSQ})$ (2.5 mg, 0.0038 mmol) was dissolved in 100 mL of toluene in an Ar-filled glovebox, and 3 mL of the solution was transferred to a cryostat UV-vis cuvette charged with a magnetic stir bar. The cuvette was sealed with a rubber septum and removed from the glovebox. With slow stirring, 1 atm of dry O_2 was bubbled gently into the solution through a needle for 5 min at room temperature. Electronic absorption spectra were collected every 15 min until no further spectral changes were observed (~ 27 h).

For the $^1\text{H NMR}$ spectroscopy and GC measurements, $[\text{PhTt}^{\text{tBu}}]\text{Ni}(\text{phenSQ})$ (30 mg, 0.045 mmol) was dissolved in 10 mL of toluene in a 100 mL Schlenk flask charged with a magnetic stir bar. The solution was removed from the glovebox and 1 atm of dry O_2 was bubbled into the solution through a needle for 5 min. Then, a balloon filled with dry O_2 was connected to the flask through a needle and a syringe. The solution was stirred for 36 h and subsequently concentrated to 2–3 mL in vacuo, and then 0.5 M HCl (2 mL, 0.5 mmol) was added. After the mixture was stirred for 5 min, 15 mL of H_2O was added and the sample was extracted with ethyl acetate (3×20 mL). The organic extracts were combined and dried over anhydrous Na_2SO_4 . After removal of ethyl acetate in vacuo, the products were obtained and analyzed by $^1\text{H NMR}$ spectroscopy (CDCl_3) and GC.

2.6. Examining the Reaction of $[\text{PhTt}^{\text{tBu}}]\text{Ni}(3,5\text{-DBSQ})$ with O_2 by Electronic Absorption Spectroscopy. $[\text{PhTt}^{\text{tBu}}]\text{Ni}(3,5\text{-DBSQ})$ (10.5 mg, 0.0155 mmol) was dissolved in 100 mL of toluene in an Ar-filled glovebox. A 3 mL aliquot of the solution was transferred to a cryostat UV-vis cuvette charged with a magnetic stir bar. The cuvette was sealed with a rubber septum and removed from the glovebox. With gentle stirring, 1 atm of dry O_2 was bubbled gently into the solution through a needle for 5 min at room temperature. Electronic absorption spectra were collected every 15 min over a 12 h period. No spectral changes were observed.

2.7. Physical Methods. NMR spectra were recorded on a Bruker AVIII 400 spectrometer. Chemical shifts (δ) were referenced to residual protons in the deuterated solvents. Electronic absorption spectra were recorded on a Varian Cary 50 UV-vis spectrophotometer using screw-top quartz cuvettes with a 1 cm path length. Solution-state magnetic moments were determined using the Evans method.^{39–41} LIFDI-MS^{42,43} was performed on a Waters GCT Premier mass spectrometer. The static magnetic properties of $[\text{PhTt}^{\text{tBu}}]\text{Fe}(\text{phenSQ})$, $[\text{PhTt}^{\text{tBu}}]\text{Ni}(\text{phenSQ})$, and $[\text{PhTt}^{\text{tBu}}]\text{Ni}(3,5\text{-DBSQ})$ were measured on samples of ground crystals using a Quantum Design MPMS-XL SQUID magnetometer operating over the temperature

range 1.8–400 K at a 1000 Oe direct-current field. The data were corrected for diamagnetic contributions using Pascal constants.

Low-field (0.04 T), variable-temperature (5–200 K) Mössbauer spectra were recorded on a closed-cycle refrigerator spectrometer, model CCR4K, equipped with a 0.04 T permanent magnet, maintaining temperatures between 5 and 300 K. The samples consisted of solid powders (or crystalline material) suspended in Nujol, placed in Delrin 1.00 mL cups, and frozen in liquid nitrogen. The isomer shifts are quoted at 5 K with respect to the iron metal spectra recorded at 298 K. Mössbauer spectra were analyzed using the software WMOSS (Thomas Kent, See Co., Edina, MN).

Electrochemical experiments were performed using a CHI-620D potentiostat/galvanostat under an N₂ atmosphere. Cyclic voltammetry (CV) and differential pulse voltammetry (DPV) were performed using a standard three-electrode configuration. The working electrode was a polished glassy carbon electrode (GCE; 3.0 mm diameter, CH Instruments), the auxiliary electrode was a platinum wire, and a Ag⁺-coated silver wire was used as a pseudoreference electrode. Decamethylferrocene (Fc^{*}; 1 mM) was used as the internal standard, and all potentials were referenced to Fc⁺/Fc through the relationship Fc⁺/Fc = 427 mV + Fc^{*}/Fc.⁴⁴

Single-crystal XRD data were obtained by mounting crystals using viscous oil onto plastic mesh and cooling them to the data collection temperature. Data were collected on a Bruker-AXS APEX II CCD diffractometer with graphite-monochromated Mo K α radiation (λ = 0.71073 Å). Unit cell parameters were obtained from 36 data frames, 0.3° ω , from three different sections of the Ewald sphere. The data sets were treated with absorption corrections based on redundant multiscan data. The systematic absences and unit cell parameters were consistent with Cc and C2/c for [PhTt^{tBu}]Ni(3,5-DBSQ) and, uniquely, with Pbc_a for [PhTt^{tBu}]NiI and with P2₁/n for [PhTt^{tBu}]Ni(PhenSQ). The solution in the centrosymmetric space group option, C2/c, for [PhTt^{tBu}]Ni(3,5-DBSQ) yielded chemically reasonable and computationally stable results of refinement. The structures were solved using direct methods and refined with full-matrix least-squares procedures on F². The iodine atom in [PhTt^{tBu}]NiI was found to be disordered in two positions with a refined site occupancy ratio of 75:25. Slight disorder was observed in a *tert*-butyl group in [PhTt^{tBu}]Ni(3,5-DBSQ) but could not be modeled satisfactorily. The disordered groups were refined with three-dimensional U_{ij} rigid-group restraints. All non-hydrogen atoms were refined with anisotropic displacement parameters. All hydrogen atoms were treated as idealized contributions. Atomic scattering factors are contained in the SHELXL 2013–2014 program libraries.⁴⁵ The CIFs have been deposited with the Cambridge Crystallographic Database as CCDC 1541366–1541368.

2.8. Computational Methods. Computational models were generated for each [PhTt^{tBu}]M^{II}SQ complex and analyzed against the available experimental data. Unless otherwise stated, the initial atomic coordinates for each [PhTt^{tBu}]M^{II}SQ model were imported from crystallographic data. DFT geometry optimizations and single-point calculations were performed with the ORCA, version 2.9.0 or 2.9.1, software package developed by Dr. Frank Neese.⁴⁶ Both high-spin and low-spin M^{II} models of each complex with a semiquinone radical ligand were considered, and the spin multiplicity of the complex was specified, rather than metal and ligand oxidation states. Metal atoms and the immediately ligated oxygen and sulfur atoms were described with Ahlrich's polarized triple- ζ -valence⁴⁷ basis set, while the remaining atoms were modeled with the polarized split-valence basis set.⁴⁸ For each spin state, computations were carried out using the spin-unrestricted formalism and either Becke's three-parameter hybrid functional for exchange along with the Lee–Yang–Parr functional for correlation (B3LYP)^{49,50} or Becke's functional for exchange along with Perdew's functional for correlation (BP86).^{51–53} Tight self-consistent-field convergence criteria were specified with an integration grid of 302 Lebedev points. For further analyses of the computed electronic structures, single-point DFT and time-dependent DFT (TD-DFT) calculations were performed on the optimized geometries. The TD-DFT results were used to simulate absorption spectra, whereby each of the 40 computed transitions was

modeled as a Gaussian band with a full width at half-maximum of 2500 cm⁻¹.

2.8.1. [PhTt^{tBu}]Fe(phenSQ). Starting coordinates for the initial models of [PhTt^{tBu}]Fe(phenSQ) were taken from X-ray crystallographic data. Because the magnetic susceptibility [$\mu_{\text{eff}} = 4.65(2) \mu_{\text{B}}$] and electronic absorption data indicate a high-spin metal center, the spin state of this complex was set to $S = 3/2$ (high-spin iron(II) coupled antiferromagnetically to an SQ⁻ ligand radical, models Fe(phenSQ)1 [B3LYP] and Fe(phenSQ)2 [BP86]). Because model Fe(phenSQ)1 converged to an unreasonable electronic structure, a third $S = 3/2$ model was generated using the optimized geometry and molecular orbital (MO) descriptions from Fe(phenSQ)2 as the starting point for a geometry optimization with the B3LYP functional [model Fe(phenSQ)3]. Mössbauer parameters were derived for Fe(phenSQ)3 using the same functionals and basis sets as described above. The DFT calibration for the isomer shift (mm/s) relative to α -iron at 295 K (eq 1) was performed using experimental data for a test set of molecules, as was previously described.⁵⁴

$$\delta = \alpha(\rho_0 - C) + \beta = -0.298(\rho_0 - 11580) + 1.118 \quad (1)$$

The computed charge density at the iron nucleus, $\rho(0)$, for Fe(phenSQ)3 from this calculation was 11581.0971, which yields $\delta = 0.791$ mm/s using eq 1. The same DFT calculation yielded a quadrupole splitting of $\Delta E_{\text{Q}} = 2.486$ mm/s.

2.8.2. [PhTt^{tBu}]Ni(phenSQ). The starting coordinates for the initial model of [PhTt^{tBu}]Ni(phenSQ) were taken from X-ray crystallographic data. Because the magnetic susceptibility measurement [$\mu_{\text{eff}} = 2.18(3) \mu_{\text{B}}$] indicates an $S = 1/2$ system, the spin state of the complex was modeled as $S = 1/2$ (high-spin nickel(II) coupled antiferromagnetically to an SQ⁻ ligand radical or low-spin nickel(II) coordinated by SQ⁻, models Ni(phenSQ)1 [B3LYP] and Ni(phenSQ)2 [BP86]). Because model Ni(phenSQ)1 converged to an unreasonable electronic structure, a third $S = 1/2$ model was generated using the optimized geometry and MO descriptions from Ni(phenSQ)2 as the starting point for a geometry optimization with the B3LYP functional [model Ni(phenSQ)3].

2.8.3. [PhTt^{tBu}]Ni(3,5-DBSQ). The starting coordinates for models of [PhTt^{tBu}]Ni(3,5-DBSQ) were taken from X-ray crystallographic data. The spin state of this complex was set to $S = 1/2$ (high-spin nickel(II) coupled antiferromagnetically to an SQ⁻ ligand radical or low-spin nickel(II) coordinated by SQ⁻, models Ni(3,5-DBSQ)1 [B3LYP] and Ni(3,5-DBSQ)2 [BP86]). Because model Ni(3,5-DBSQ)1 converged to an unreasonable electronic structure, a third $S = 1/2$ model was generated using the optimized geometry and MO descriptions from Ni(3,5-DBSQ)2 as the starting point for a geometry optimization with the B3LYP functional [model Ni(3,5-DBSQ)3].

3. RESULTS AND DISCUSSION

3.1. Electronic and Magnetic Properties of [PhTt^{tBu}]Fe(phenSQ). To further interrogate the electronic structure of [PhTt^{tBu}]Fe(phenSQ), solid-state Mössbauer spectra were collected in an applied field of 0.04 T at a range of temperatures. The zero-field spectrum recorded at 100 K is displayed in Figure 2. The spectra at 6–100 K exhibit a single sharp quadrupole doublet, with an isomer shift (δ) of 0.92 mm/s and a quadrupole splitting (ΔE_{Q}) of 2.29 mm/s, which are consistent with high-spin iron(II). Temperatures up to 200 K did not significantly affect the quadrupole splitting. A five-coordinate high-spin ferrous complex with redox-innocent ligands, {[PhTt^{tBu}]FeCl}₂, which was previously characterized in our laboratories,⁵⁵ exhibited Mössbauer parameters of $\delta = 0.96$ mm/s and $\Delta E_{\text{Q}} = 3.45$ mm/s, similar to those of [PhTt^{tBu}]Fe(phenSQ). Recently, Fiedler, Popescu, and co-workers have explored the oxidation of iron(II) catecolate complexes with Mössbauer spectroscopy, showing that metal-based oxidation to iron(III) catechololate leads to a significantly lower isomer shift (0.5 mm/s).⁵⁶ Thus, the Mössbauer data of

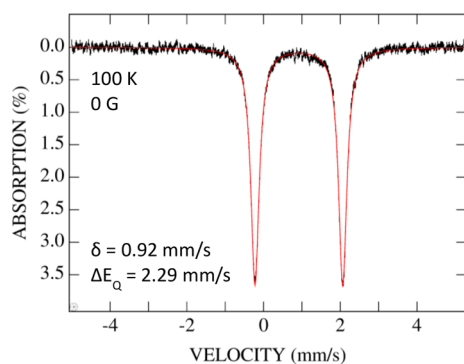


Figure 2. Zero-field Mössbauer spectrum of $[\text{PhTt}^{\text{tBu}}]\text{Fe}(\text{phenSQ})$ at 100 K. The solid red line is a least-squares fit obtained with the parameters shown.

$[\text{PhTt}^{\text{tBu}}]\text{Fe}(\text{phenSQ})$ strongly support its description as a high-spin iron(II) semiquinone species.

To study the magnetic interaction between the high-spin iron(II) and the *o*-semiquinone ligand, the temperature-dependent magnetic susceptibility of $[\text{PhTt}^{\text{tBu}}]\text{Fe}(\text{phenSQ})$ in the solid state was probed by SQUID magnetometry. As shown in Figure 3, the χT value of $2.58 \text{ cm}^3 \text{ K mol}^{-1}$ at 300 K ($\mu_{\text{eff}} =$

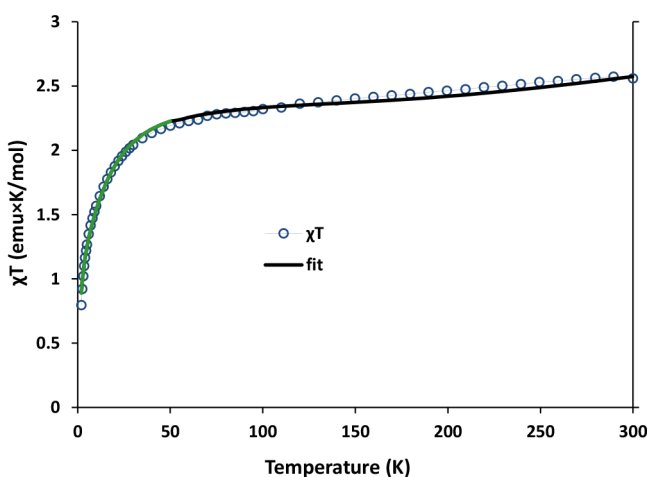


Figure 3. Temperature dependence of χT (blue circles) for $[\text{PhTt}^{\text{tBu}}]\text{Fe}(\text{phenSQ})$. The susceptibility data were fitted (black and green lines) as described in the text, yielding $J = -127 \text{ cm}^{-1}$ ($g = 2.22$), $D = +14.5 \text{ cm}^{-1}$, $E = 0.001 \text{ cm}^{-1}$, and $zJ = -0.23 \text{ cm}^{-1}$.

$4.54 \mu_{\text{B}}$) comports with the solution magnetic moment at room temperature [$\mu_{\text{eff}} = 4.65(2) \mu_{\text{B}}$], confirming the same spin state in the solid state and in solution. As the temperature was lowered from 300 to 50 K, the χT value slowly decreased to $2.19 \text{ cm}^3 \text{ K mol}^{-1}$, which is slightly higher than the spin-only value of $1.88 \text{ cm}^3 \text{ K mol}^{-1}$ for an $S = 3/2$, $g = 2.0$ system but much lower than what is expected for the uncoupled (i.e., $S = 2$ and $1/2$) system of $3.38 \text{ cm}^3 \text{ K mol}^{-1}$. Thus, $[\text{PhTt}^{\text{tBu}}]\text{Fe}(\text{phenSQ})$ adopts an $S = 3/2$ ground state derived from antiferromagnetic coupling between the high-spin iron(II) ($S = 2$) and the *o*-semiquinone radical ($S = 1/2$). The increase in χT as the temperature was raised from 50 to 300 K is likely due to the thermal population of the $S = 5/2$ excited state. Interestingly, Fiedler's mononuclear five-coordinate iron(II) *p*-semiquinone complexes exhibit ferromagnetic coupling between the high-spin iron(II) center and the *p*-semiquinone radical to yield an $S = 5/2$ ground state, as indicated by electron

paramagnetic resonance (EPR) and DFT data.^{57,58} The ferromagnetic coupling observed in the iron(II) *p*-semiquinone complexes (DFT-computed J values of $\sim 65 \text{ cm}^{-1}$, $H = -2J\mathbf{S}_1 \cdot \mathbf{S}_2$) was attributed to the orthogonal orientation of the magnetic orbitals.

Below 50 K, the χT values dropped sharply, which may be attributed to zero-field splitting (ZFS) and/or intermolecular interactions. The field-dependent magnetization data collected at 1.8 K (Figure S7) slowly increased at lower fields, which is indicative of intermolecular antiferromagnetic interactions. At fields above 5 T, magnetization approached saturation at $2.1 \mu_{\text{B}}$, well below the expected value, which is also indicative of ZFS and/or intermolecular interactions. The susceptibility data were fitted to the Hamiltonian $H = -2J(\mathbf{S}_1 \cdot \mathbf{S}_2) + DS_z^2 + E(S_x^2 - S_y^2) + g\beta\mathbf{B} \cdot \mathbf{S}$ using PHI software.⁵⁹ The χT values in the high-temperature regime (300–50 K) were used to calculate a coupling constant of -127 cm^{-1} with $g = 2.22$. Fits of the low-temperature range were used to estimate the ZFS parameters of the iron(II) ion (D and E) and intermolecular interactions (zJ). Best fits were obtained for $D = +14.5 \text{ cm}^{-1}$, $E = 0.001 \text{ cm}^{-1}$, and $zJ = -0.23 \text{ cm}^{-1}$. No satisfactory fits were obtained without including intermolecular interactions. The field-dependent magnetization curves at different temperatures (1.8–4.5 K) are nonsuperimposable, indicating the presence of ZFS (Figure S8).

DFT calculations were performed using the broken-symmetry approach to provide a detailed description of the electronic structure of $[\text{PhTt}^{\text{tBu}}]\text{Fe}(\text{phenSQ})$. Starting from the molecular structure of $[\text{PhTt}^{\text{tBu}}]\text{Fe}(\text{phenSQ})$ determined by XRD, geometry optimizations for the $S = 3/2$ spin state were performed using both the BP86 and B3LYP functionals. The metric parameters and electronic structure descriptions obtained from the experimental data and DFT calculations are provided in Table 1. While model Fe(phenSQ)1 fails to

Table 1. Selected Bond Distances (Å) for $[\text{PhTt}^{\text{tBu}}]\text{Fe}(\text{phenSQ})$ Obtained by XRD and DFT, along with Electronic Structure Descriptions Derived from Experimental Data and DFT Calculations^a

bond distance	XRD	Fe(phenSQ)1	Fe(phenSQ)	Fe(phenSQ)
		(B3LYP, $S = 3/2$)	2 (BP86, $S = 3/2$)	3 (B3LYP, $S = 3/2$)
Fe1–O1	2.064(2)	1.932	2.062	2.150
Fe1–O2	2.015(2)	1.926	2.033	2.029
O1–C22	1.285(2)	1.311	1.302	1.279
O2–C35	1.285(2)	1.311	1.304	1.292
C35–C22	1.435(3)	1.412	1.444	1.446
Fe1–S2(ax)	2.388(1)	2.544	2.307	2.439
Fe1–S1(eq)	2.456(1)	2.387	2.474	2.509
Fe1–S3(eq)	2.506(1)	2.372	2.509	2.591
electronic structures	high-spin Fe ^{II} with AF-coupled SQ	intermediate-spin Fe ^{II} with F-coupled SQ	high-spin Fe ^{II} with AF-coupled SQ	high-spin Fe ^{II} with AF-coupled SQ

^aAF = antiferromagnetic. F = ferromagnetic.

predict the correct spin state of iron, the geometries and ground-state electronic structures of models Fe(phenSQ)2 and Fe(phenSQ)3 are consistent with the experimental data. However, because the TD-DFT-calculated electronic absorption spectrum for Fe(phenSQ)2 agrees poorly with the experimental data (Figure S11), only the results obtained for model Fe(phenSQ)3 will be discussed further.

The DFT-computed Mössbauer parameters for Fe(phenSQ)₃, $\delta = 0.79$ mm/s and $\Delta E_Q = 2.49$ mm/s, are in good agreement with the experimental isomer shift $\delta = 0.92$ mm/s and quadrupole splitting $\Delta E_Q = 2.29$ mm/s (Table 2). Likewise, the calculated coupling constant, $J = -79.7$ cm⁻¹, agrees reasonably well with the experimental value, $J = -127$ cm⁻¹ (Table 2).

Table 2. Experimental and DFT-Calculated Mössbauer Parameters and Coupling Constant, *J*, Derived from Model Fe(phenSQ)₃

	δ (mm/s)	ΔE_Q (mm/s)	<i>J</i> (cm ⁻¹)
experimental	0.92	2.29	-127
calculated	0.79	2.49	-79.7

The TD-DFT-calculated electronic absorption spectrum for model Fe(phenSQ)₃ is in good agreement with the experimental spectrum (Figure 4). The transitions associated

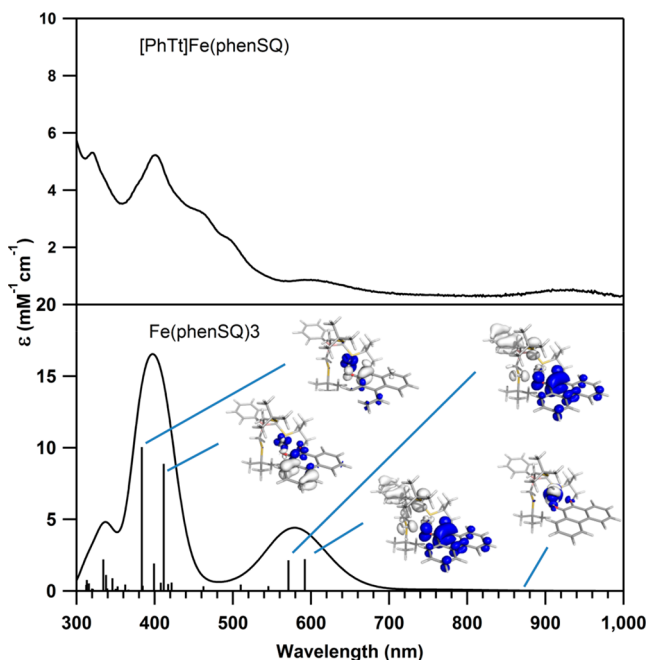


Figure 4. Comparison of the experimental electronic absorption spectrum of [PhTt^{tBu}]Fe(phenSQ) and the TD-DFT-calculated spectrum for model Fe(phenSQ)₃. EDDMs for the relevant transitions are shown on top of the computed spectrum.

with the major features in the computed spectrum were assigned on the basis of electron density difference maps (EDDMs; Figures 4 and S16). The transitions responsible for the two intense features at 384 nm (16736 M⁻¹ cm⁻¹) and 412 nm (14784 M⁻¹ cm⁻¹) have primarily phenSQ-to-Fe^{II} charge-transfer character and both phenSQ-to-Fe^{II} charge-transfer and phenSQ $\pi \rightarrow \pi^*$ character, respectively. The transitions associated with the weaker features at 571 nm (3575 M⁻¹ cm⁻¹) and 592 nm (3693 M⁻¹ cm⁻¹) have large contributions from Fe^{II}-to-phenSQ and [PhTt^{tBu}]-to-phenSQ charge-transfer excitations. These features match with the experimental transition at 600 nm (868 M⁻¹ cm⁻¹). Finally, the Fe^{II} d_{xz}/d_{yz} to $d_{x^2-y^2}$ transition gives rise to the weak feature at 874 nm (4 M⁻¹ cm⁻¹) in the calculated spectrum, which corresponds to

the broad band at 935 nm (539 M⁻¹ cm⁻¹) in the experimental spectrum.

The good agreement between the geometric structures and spectroscopic data obtained experimentally for [PhTt^{tBu}]Fe(phenSQ) and predicted computationally for model Fe(phenSQ)₃ warrants a closer inspection of the calculated electronic structure. The qualitative MO diagram for model Fe(phenSQ)₃ derived from the DFT results (Figure 5) reveals that the iron(II) ion is high-spin ($S = 2$), with one electron pair occupying the Fe d_{yz} -based MO and the four unpaired spin-up electrons occupying the remaining Fe d-based MOs. The spin-up electron in the Fe d_{xz} -based MO is coupled to the spin-down electron in the SQ π^* -based MO with a modest spatial overlap of $S = 0.28$, giving rise to the antiferromagnetic coupling between the high-spin iron(II) and the SQ radical observed by SQUID magnetometry.

3.2. O₂ Reactivity of [PhTt^{tBu}]Fe(phenSQ). Numerous iron(III) catecholate complexes modeling the reactivity of intradiol catechol dioxygenases have been reported over the last 30 years.^{15–17,60–68} While the intradiol cleaving reactivity of the enzymes and the model complexes was often attributed to the iron(II) semiquinonate character within the iron(III) catecholate species, we are unaware of any well-characterized iron(II) semiquinonate species exhibiting intradiol cleaving reactivity. Thus, our well-characterized iron(II) *o*-semiquinonate complex, [PhTt^{tBu}]Fe(phenSQ), afforded a unique opportunity to test the “iron(II) semiquinonate” mechanistic hypothesis by reacting it with O₂.

Dry O₂ was introduced to a toluene solution of [PhTt^{tBu}]Fe(phenSQ) at -78 °C, and the reaction mixture was allowed to warm to ambient temperature. The mass spectrum of the products (Figure 6a) was compared to the calculated mass spectra of phenanthrenequinone (Figure 6b) and diphenic anhydride (Figure 6c). The results obtained are consistent with the formation of diphenic anhydride, the intradiol cleavage product, as well as phenanthrenequinone. To further characterize the organic products, the reaction was performed on a preparative scale. The organic products were dissociated from the iron via the addition of 0.5 M HCl followed by extraction into ethyl acetate. Signals of diphenic anhydride were identifiable in the ¹H NMR spectrum of the products, although they partially overlapped with the signals of other products (Figure 6d). The yields of diphenic anhydride (16%) and phenanthrenequinone (4%) were determined by GC (Figure S22). The reaction of [PhTt^{tBu}]Fe(phenSQ) with O₂ is depicted in Scheme 3. Notably, the formation of diphenic anhydride through oxygenation of [PhTt^{tBu}]Fe(phenSQ) represents the first example of intradiol cleaving reactivity of a synthetic iron(II) semiquinonate complex. Furthermore, it validates our previous assertion that the observed intermediate(s) of the reaction of [PhTt^{tBu}]Fe(phenSQ) with O₂ at low temperature³⁶ is relevant to the intradiol reactivity. The reason for the low yield of the intradiol cleavage product is not clear. We propose that boronic esters derived from the phenSQ ligand may be generated because a similar product was identified in the oxygenation reaction of [PhTt^{tBu}]Co(3,5-DBSQ).³⁶ Indeed, in addition to diphenic anhydride and phenanthrenequinone, signals consistent with 2-phenylphenanthro[9,10-*d*][1,3,2]dioxaborole (*m/z* 296.10) and 2-phenoxyphenanthro[9,10-*d*][1,3,2]dioxaborole (*m/z* 312.12) were observed in the LIFDI-MS spectrum collected on the reaction mixture of [PhTt^{tBu}]Fe(phenSQ) and O₂ without treatment by acid (Figure S24).

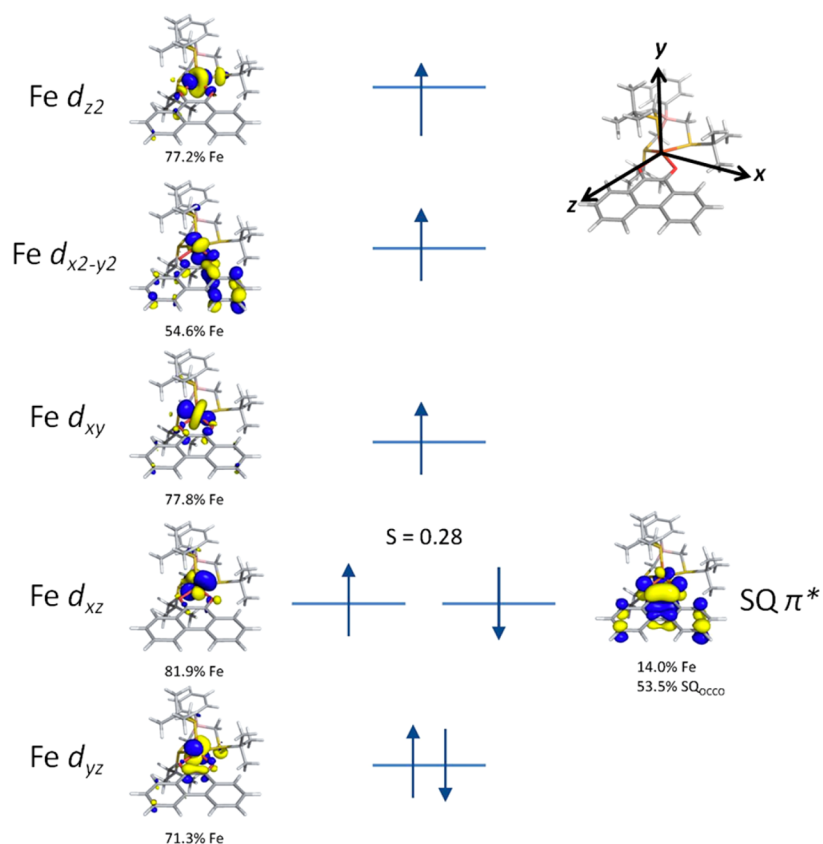


Figure 5. Qualitative MO diagram derived from a DFT calculation for model Fe(phenSQ)₃.

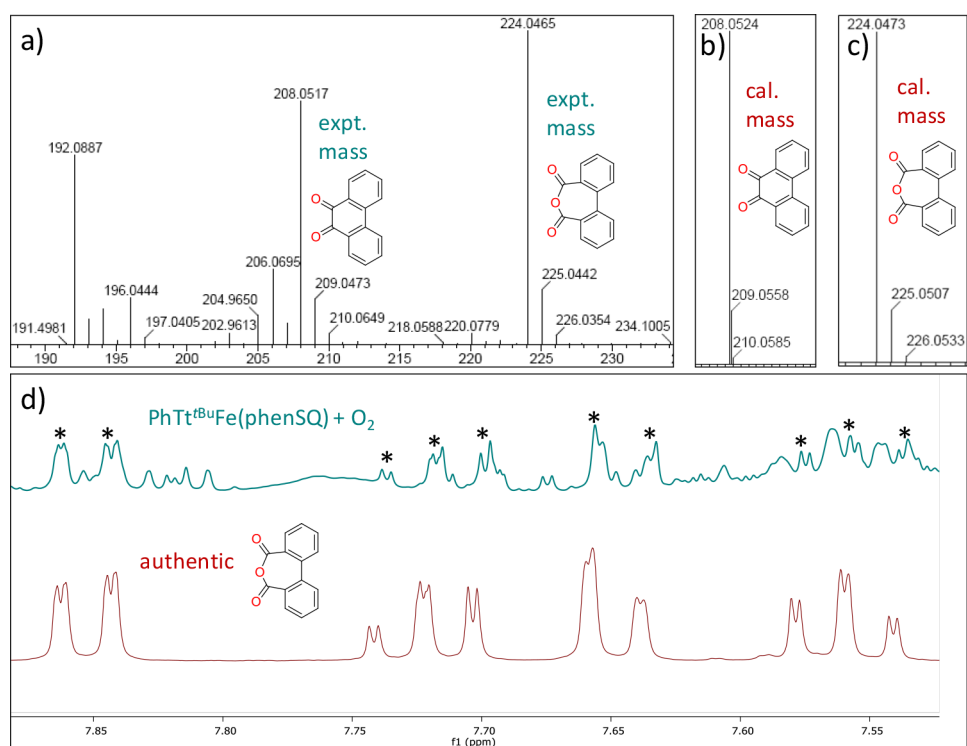
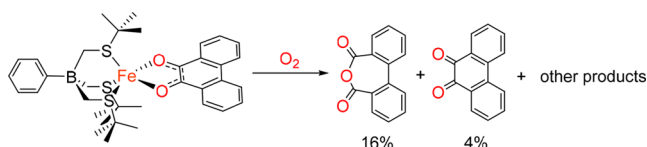


Figure 6. Analysis of the organic products of the reaction of [PhTt^{tBu}]Fe(phenSQ) with O₂. (a) LIFDI-MS spectrum of the organic products. (b) Calculated mass spectrum of phenanthrenequinone. (c) Calculated mass spectrum of diphenic anhydride. (d) ¹H NMR spectra of the organic products (top) and authentic diphenic anhydride (bottom).

3.3. Synthesis and X-ray Structures of [PhTt^{tBu}]Ni(phenSQ) and [PhTt^{tBu}]Ni(3,5-DBSQ). Inspired by the

findings of the intradiol cleaving reactivity of [PhTt^{tBu}]Fe(phenSQ), as well as the previously reported intradiol reactivity

Scheme 3. Reaction of $[\text{PhTt}^{\text{tBu}}]\text{Fe}(\text{phenSQ})$ with O_2 

of $[\text{PhTt}^{\text{tBu}}]\text{Co}(3,5\text{-DBSQ})$,³⁶ we sought to assess the role of the metal ion in directing O_2 reactivity. To this end, we prepared, characterized, and explored the O_2 reactivity of two nickel(II) semiquinonate complexes, $[\text{PhTt}^{\text{tBu}}]\text{Ni}(\text{phenSQ})$ and $[\text{PhTt}^{\text{tBu}}]\text{Ni}(3,5\text{-DBSQ})$.

The strategy employed for the preparation of $[\text{PhTt}^{\text{tBu}}]\text{Ni}(\text{phenSQ})$ and $[\text{PhTt}^{\text{tBu}}]\text{Ni}(3,5\text{-DBSQ})$ was similar to that used for the preparation of $[\text{PhTt}^{\text{tBu}}]\text{Fe}(\text{phenSQ})$. Metathesis of $[\text{PhTt}^{\text{tBu}}]\text{NiI}$ with $\text{Ti}(\text{phenSQ})$ yielded $[\text{PhTt}^{\text{tBu}}]\text{Ni}(\text{phenSQ})$ in 80% yield. Metathesis of $[\text{PhTt}^{\text{tBu}}]\text{NiI}$ with $\text{Ti}(3,5\text{-DBSQ})$ yielded $[\text{PhTt}^{\text{tBu}}]\text{Ni}(3,5\text{-DBSQ})$ in 85% yield. Both complexes are five-coordinate, as revealed by their X-ray crystal structures, with the phenSQ and 3,5-DBSQ ligands binding to the nickel center in a bidentate fashion (Figure 7). $[\text{PhTt}^{\text{tBu}}]\text{Ni}(\text{phenSQ})$ adopts a square-pyramidal geometry ($\tau_5 = 0.00$), while the geometry of $[\text{PhTt}^{\text{tBu}}]\text{Ni}(3,5\text{-DBSQ})$ is distorted square-pyramidal ($\tau_5 = 0.34$).⁶⁹ Selected bond distances are listed in Table 3. The average C–O distances for $[\text{PhTt}^{\text{tBu}}]\text{Ni}(\text{phenSQ})$ and $[\text{PhTt}^{\text{tBu}}]\text{Ni}(3,5\text{-DBSQ})$ are 1.283(3) and 1.285(2) Å, respectively, characteristic of semiquinonate ligands (1.27–1.31 Å). The average Ni–O distances for $[\text{PhTt}^{\text{tBu}}]\text{Ni}(\text{phenSQ})$ and $[\text{PhTt}^{\text{tBu}}]\text{Ni}(3,5\text{-DBSQ})$ are 2.001(2) and 1.999(1) Å, respectively. These distances are nearly identical with the average Ni–O distance [2.002(1) Å] of a trigonal-bipyramidal high-spin nickel(II) semiquinonate complex reported by Shultz and co-workers,⁷⁰ indicating that both $[\text{PhTt}^{\text{tBu}}]\text{Ni}(\text{phenSQ})$ and $[\text{PhTt}^{\text{tBu}}]\text{Ni}(3,5\text{-DBSQ})$ are high-spin ($S = 1$) nickel(II) complexes.

3.4. Electronic and Magnetic Properties of $[\text{PhTt}^{\text{tBu}}]\text{Ni}(\text{phenSQ})$ and $[\text{PhTt}^{\text{tBu}}]\text{Ni}(3,5\text{-DBSQ})$. The signals in the ^1H NMR spectra of both nickel semiquinonate complexes are broad and paramagnetically shifted, reflecting the paramagnetic character of the complexes. The electronic absorption spectrum of $[\text{PhTt}^{\text{tBu}}]\text{Ni}(\text{phenSQ})$ shows LF transitions at 846 nm ($710 \text{ M}^{-1} \text{ cm}^{-1}$) and 966 nm (shoulder). Similarly, $[\text{PhTt}^{\text{tBu}}]\text{Ni}(3,5\text{-DBSQ})$ exhibits LF transitions at 842 nm ($823 \text{ M}^{-1} \text{ cm}^{-1}$) and 966 nm (shoulder), as shown in Figure 8.

The aforementioned LF transitions are present only when the Ni^{II} ion is high-spin ($S = 1$). Indeed, LF transitions of previously reported five-coordinate high-spin nickel(II) complexes of tris(thioether) borate ligands are found at similar wavelengths [866 nm ($54 \text{ M}^{-1} \text{ cm}^{-1}$) for $[\text{PhTt}^{\text{tBu}}]\text{Ni}(\text{NO}_3)$ ⁷¹ and 845 nm ($350 \text{ M}^{-1} \text{ cm}^{-1}$) for $[\text{PhTt}^{\text{Ad}}]\text{Ni}(\text{O}_2)$ ⁷²].

Table 3. Selected Bond Distances (Å) for $[\text{PhTt}^{\text{tBu}}]\text{Ni}(\text{phenSQ})$ and $[\text{PhTt}^{\text{tBu}}]\text{Ni}(3,5\text{-DBSQ})$ Obtained by XRD and DFT, along with Electronic Structure Descriptions Derived from Experimental Data and DFT Calculations^a

bond distance	XRD	Ni(phenSQ)	Ni(phenSQ)	Ni(phenSQ)
		1 (B3LYP, $S = 1/2$)	2 (BP86, $S = 1/2$)	3 (B3LYP, $S = 1/2$)
Ni–O1	2.015(2)	2.017	2.043	2.052
Ni–O2	1.986(2)	1.994	2.033	2.050
O1–C22	1.280(3)	1.286	1.293	1.282
O2–C35	1.285(3)	1.288	1.293	1.283
C35–C22	1.433(3)	1.440	1.452	1.447
Ni1–S2(ax)	2.303(1)	2.482	2.296	2.373
Ni1–S1(eq)	2.381(1)	2.398	2.384	2.441
Ni1–S3(eq)	2.358(1)	2.357	2.379	2.438
electronic structures	high-spin Ni^{II} with AF-coupled SQ	low-spin Ni^{II} with SQ	high-spin Ni^{II} with AF-coupled SQ	high-spin Ni^{II} with AF-coupled SQ

bond distance	XRD	Ni(3,5-DBSQ)1	Ni(3,5-DBSQ)2	Ni(3,5-DBSQ)3
		(B3LYP, $S = 1/2$)	(BP86, $S = 1/2$)	(B3LYP, $S = 1/2$)
Ni1–O1	2.026(1)	2.007	2.064	2.084
Ni1–O2	1.971(1)	1.986	1.986	2.017
O1–C22	1.282(2)	1.293	1.299	1.285
O2–C27	1.287(2)	1.290	1.302	1.287
C22–C27	1.458(2)	1.464	1.472	1.472
Ni1–S2(ax)	2.301(1)	2.506	2.293	2.381
Ni1–S1(eq)	2.382(1)	2.396	2.372	2.435
Ni1–S3(eq)	2.393(1)	2.362	2.410	2.455
electronic structures	high-spin Ni^{II} with AF-coupled SQ	low-spin Ni^{II} with SQ	high-spin Ni^{II} with AF-coupled SQ	high-spin Ni^{II} with AF-coupled SQ

^aAF = antiferromagnetic. F = ferromagnetic.

The temperature-dependent magnetic properties of the nickel(II) semiquinonate complexes were examined using SQUID magnetometry (Figure 9). For $[\text{PhTt}^{\text{tBu}}]\text{Ni}(3,5\text{-DBSQ})$, the χT value is $0.52 \text{ cm}^3 \text{ K mol}^{-1}$ at 300 K, corresponding to $\mu_{\text{eff}} = 2.03 \mu_{\text{B}}$, which is consistent with the solution μ_{eff} of $2.25 \mu_{\text{B}}$ at room temperature. This μ_{eff} value is slightly higher than the spin-only value of $1.73 \mu_{\text{B}}$ expected for an $S = 1/2$ ground state but much lower than that for the uncoupled ($S = 1$ and $1/2$) system ($\mu_{\text{eff}} = 3.32 \mu_{\text{B}}$), suggesting strong antiferromagnetic coupling between the high-spin Ni^{II} ($S = 1$) and 3,5-DBSQ radical ($S = 1/2$). The χT values are effectively constant throughout the temperature range 2–300 K, which further supports the presence of very strong antiferromagnetic coupling, leading to population of only the $S = 1/2$ state. Above 300 K, χT gradually increased because of

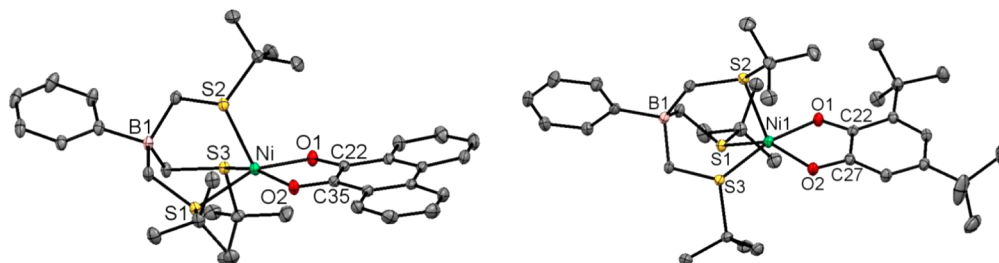


Figure 7. Crystal structures of $[\text{PhTt}^{\text{tBu}}]\text{Ni}(\text{phenSQ})$ (left) and $[\text{PhTt}^{\text{tBu}}]\text{Ni}(3,5\text{-DBSQ})$ (right).

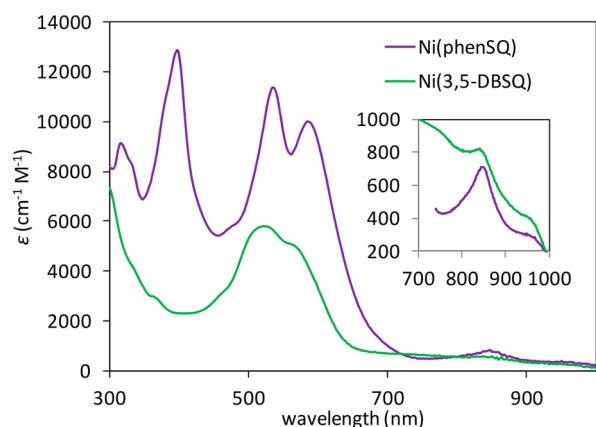


Figure 8. Electronic absorption spectra of $[\text{PhTt}^{\text{tBu}}]\text{Ni}(\text{phenSQ})$ and $[\text{PhTt}^{\text{tBu}}]\text{Ni}(3,5\text{-DBSQ})$ in toluene. The inset highlights the LF transitions.

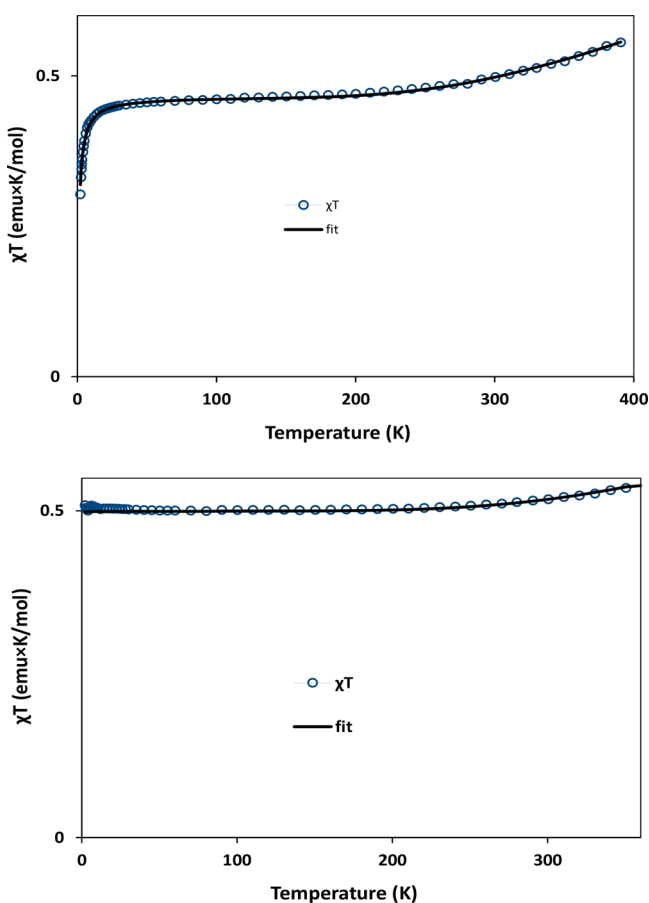


Figure 9. χT versus T plots (blue circles) for $[\text{PhTt}^{\text{tBu}}]\text{Ni}(\text{phenSQ})$ (top) and $[\text{PhTt}^{\text{tBu}}]\text{Ni}(3,5\text{-DBSQ})$ (bottom). The susceptibility data were fitted (black line) as described in the text, yielding $J = -320 \text{ cm}^{-1}$ ($g = 2.22$) and $zJ = -0.57 \text{ cm}^{-1}$ for $[\text{PhTt}^{\text{tBu}}]\text{Ni}(\text{phenSQ})$ and $J = -382 \text{ cm}^{-1}$ ($g = 2.24$) for $[\text{PhTt}^{\text{tBu}}]\text{Ni}(3,5\text{-DBSQ})$.

the thermal population of the $S = 3/2$ excited state. The field-dependent magnetization data collected at 1.8 K show saturation behavior at fields above 5 T, consistent with an $S = 1/2$ coupled ground state (Figure S9). Fitting of the susceptibility data to the Hamiltonian $H = -2J(S_1 \cdot S_2) + DS_z^2 + E(S_x^2 - S_y^2) + g\beta\mathbf{B} \cdot \mathbf{S}$ using PHI software⁵⁹ yielded a large J of -382 cm^{-1} ($g = 2.24$). Because the χT values remain constant

even at low temperature, intermolecular interactions were not considered in this fit.

Strong antiferromagnetic coupling was also observed for $[\text{PhTt}^{\text{tBu}}]\text{Ni}(\text{phenSQ})$. The room temperature μ_{eff} for $[\text{PhTt}^{\text{tBu}}]\text{Ni}(\text{phenSQ})$ in benzene- d_6 is $2.18(3) \mu_{\text{B}}$, indicating an $S = 1/2$ ground state. The χT value is $0.505 \text{ cm}^3 \text{ K mol}^{-1}$ ($\mu_{\text{eff}} = 2.0 \mu_{\text{B}}$; $g = 2.31$) at 300 K. A slightly steeper increase in χT was observed between 300 and 390 K. Additionally, below 15 K, the χT values for $[\text{PhTt}^{\text{tBu}}]\text{Ni}(\text{phenSQ})$ dropped gradually down to $0.31 \text{ cm}^3 \text{ K mol}^{-1}$ at 2 K, possibly signifying intermolecular interactions via π - π -stacking pathways in the solid-state structure. The saturation behavior of the magnetization data collected at 1.8 K further supports an $S = 1/2$ coupled ground state (Figure S10). Fitting of the susceptibility data revealed a smaller [relative to $[\text{PhTt}^{\text{tBu}}]\text{Ni}(3,5\text{-DBSQ})$] exchange coupling constant of $J = -320 \text{ cm}^{-1}$ and small intermolecular dipolar coupling, $zJ = -0.57 \text{ cm}^{-1}$ ($g = 2.22$, assuming $J \gg D$). Notably, a five-coordinate $\text{Ni}^{\text{II}}(3,5\text{-DBSQ})$ complex of a triazamacrocyclic ligand reported by Dei and co-workers⁷³ exhibits strong antiferromagnetic coupling between high-spin Ni^{II} and 3,5-DBSQ ligand with $\mu_{\text{eff}} = 1.89 \mu_{\text{B}}$. The absolute value of the coupling constant was estimated to be greater than 300 cm^{-1} because of the lack of excited-state population. Similarly, in Shultz's $\text{Tp}^{\text{Cum,Me}}\text{Ni}(\text{nitronyl nitroxide semiquinone})$, the calculated $J_{\text{Ni-SQ}}$ value is between -244 and -525 cm^{-1} .⁷⁰ To the best of our knowledge, our measurements represent the first accurate determination of coupling constants for five-coordinate high-spin nickel(II) complexes with antiferromagnetically coupled semiquinonate ligands.

Following the approach employed for $[\text{PhTt}^{\text{tBu}}]\text{Fe}(\text{phenSQ})$, broken-symmetry DFT calculations were performed for $[\text{PhTt}^{\text{tBu}}]\text{Ni}(\text{phenSQ})$ and $[\text{PhTt}^{\text{tBu}}]\text{Ni}(3,5\text{-DBSQ})$ to obtain detailed descriptions of the electronic structures and to correlate the electronic structures with the magnetic properties. Geometry optimizations based on the X-ray crystal structures were performed for the $S = 1/2$ spin ground state using both the BP86 and B3LYP functionals. When the B3LYP functional was used, the calculated geometric and electronic structures of $[\text{PhTt}^{\text{tBu}}]\text{Ni}(\text{phenSQ})$ [model Ni(phenSQ)1] and $[\text{PhTt}^{\text{tBu}}]\text{Ni}(3,5\text{-DBSQ})$ [model Ni(3,5-DBSQ)1] did not agree with the experimental data (Table 3). Although the models obtained using the BP86 functional, Ni(phenSQ)2 and Ni(3,5-DBSQ)2, accurately reproduce the experimental molecular structures and are predicted to have the correct spin distribution, the TD-DFT-calculated electronic absorption spectra are inconsistent with the experimental data (Figures S12 and S13). However, when models Ni(phenSQ)3 and Ni(3,5-DBSQ)3, exhibited geometric and electronic structures and afforded TD-DFT-calculated absorption spectra consistent with the corresponding experimental data.

The TD-DFT-calculated absorption spectrum for the Ni(phenSQ)3 model is in excellent agreement with the experimental spectrum of $[\text{PhTt}^{\text{tBu}}]\text{Ni}(\text{phenSQ})$ (Figure 10). Inspection of the EDDMs provided in Figures 10 and S17 reveals that the intense feature at 397 nm ($15967 \text{ M}^{-1} \text{ cm}^{-1}$) in the computed spectrum, which corresponds to the prominent feature at 398 nm ($12877 \text{ M}^{-1} \text{ cm}^{-1}$) in the experimental spectrum, arises from a semiquinonate intraligand transition. Toward lower energy, the transitions associated with the computationally predicted features at 547 ($3497 \text{ M}^{-1} \text{ cm}^{-1}$) and 555 nm ($4864 \text{ M}^{-1} \text{ cm}^{-1}$) have primarily Ni^{II} -to-phenSQ

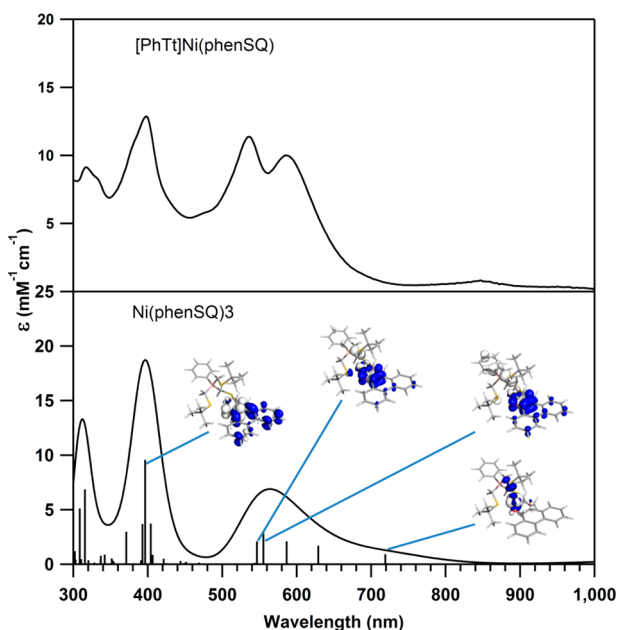


Figure 10. Comparison of the experimental absorption spectrum of $[\text{PhTt}^{\text{tBu}}]\text{Ni}(\text{phenSQ})$ and the TD-DFT calculated spectrum for model $\text{Ni}(\text{phenSQ})_3$. EDDMs for the relevant transitions are shown on top of the computed spectrum.

charge-transfer character. Lastly, the weak feature in the computed spectrum at 719 nm ($1533 \text{ M}^{-1} \text{ cm}^{-1}$), which

corresponds to the broad band at 846 nm ($710 \text{ M}^{-1} \text{ cm}^{-1}$) in the experimental spectrum, arises from a nickel(II) LF transition.

The TD-DFT calculated absorption spectrum for model $\text{Ni}(3,5\text{-DBSQ})_3$ and the experimental spectrum of $[\text{PhTt}^{\text{tBu}}]\text{Ni}(3,5\text{-DBSQ})$ also agree quite well (Figure S14). Because these spectra and the underlying transitions are similar to those of $[\text{PhTt}^{\text{tBu}}]\text{Ni}(\text{phenSQ})$ described above, they will not be discussed further.

A qualitative MO diagram for model $\text{Ni}(\text{phenSQ})_3$ derived from our DFT results is shown in Figure 11. Consistent with our experimental data, the Ni^{II} is high-spin, with two unpaired spin-up electrons occupying the $\text{Ni}(d_{z^2})$ - and $\text{Ni}(d_{x^2-y^2})$ -based MOs. The spin-up electron in the $\text{Ni}(d_{z^2})$ -based MO is coupled to the spin-down electron in the phenSQ π^* -based MO with spatial overlap of $S = 0.31$, leading to the strong antiferromagnetic coupling observed by SQUID magnetometry. The calculated coupling constant, $J = -273 \text{ cm}^{-1}$, is in good agreement with the SQUID-derived value, $J = -320 \text{ cm}^{-1}$.

As expected on the basis of the experimental and TD-DFT-computed absorption spectra, the MO diagram for model $\text{Ni}(3,5\text{-DBSQ})_3$ (Figure S15) closely resembles that obtained for $\text{Ni}(\text{phenSQ})_3$ in Figure 11. Again, the spin-up electron in the $\text{Ni}(d_{z^2})$ -based MO is coupled to the spin-down electron in the 3,5-DBSQ π^* -based MO with spatial overlap of $S = 0.31$, leading to strong antiferromagnetic coupling. The larger coupling constant calculated for this complex, $J = -282$ versus -273 cm^{-1} for $[\text{PhTt}^{\text{tBu}}]\text{Ni}(\text{phenSQ})$, agrees with our SQUID data, which show that $[\text{PhTt}^{\text{tBu}}]\text{Ni}(3,5\text{-DBSQ})$ features

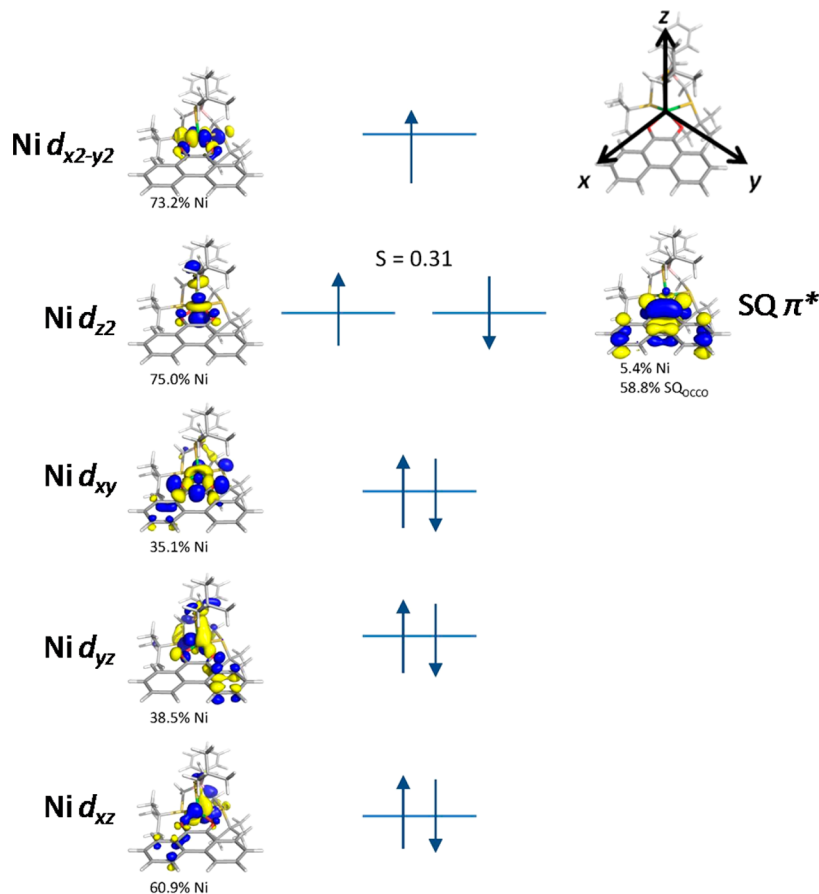


Figure 11. Qualitative MO diagram for model $\text{Ni}(\text{phenSQ})_3$ derived from the DFT results.

stronger antiferromagnetic coupling between the Ni^{II} ion and the semiquinone ligand. Similarly strong antiferromagnetic coupling between high-spin nickel(II) and a ligand derived radical, superoxide, has been proposed to best describe the electronic structures of nickel–dioxygen adducts, including those prepared directly from nickel(I) and O₂.^{74,75}

3.5. O₂ Reactivity of [PhTt^{tBu}]Ni(phenSQ) and [PhTt^{tBu}]Ni(3,5-DBSQ). With a thorough understanding of the electronic structures of [PhTt^{tBu}]Ni(phenSQ) and [PhTt^{tBu}]Ni(3,5-DBSQ) in hand, their O₂ reactivity was investigated. Stirring a toluene solution of [PhTt^{tBu}]Ni(phenSQ) under O₂ at room temperature resulted in the slow decomposition of the complex, as indicated by the gradual loss of electronic absorption bands at 536, 586, and 846 nm (Figure 12). To

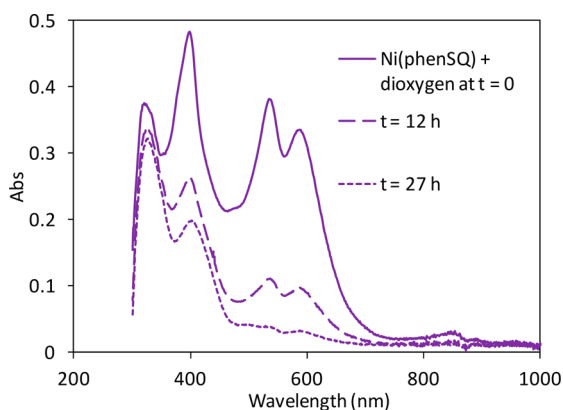


Figure 12. Decomposition of [PhTt^{tBu}]Ni(phenSQ) in toluene under an O₂ atmosphere at room temperature monitored by electronic absorption spectroscopy.

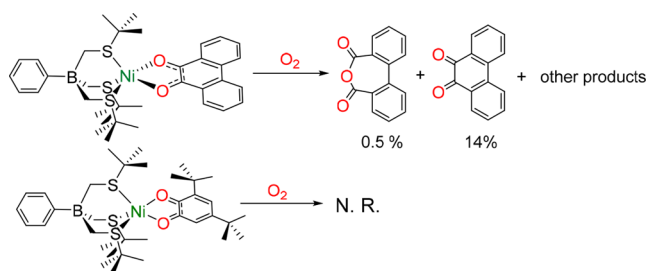
identify the organic products, the reaction of [PhTt^{tBu}]Ni(phenSQ) with O₂ was conducted on a preparative scale and monitored by electronic absorption spectroscopy. After complete decomposition of [PhTt^{tBu}]Ni(phenSQ), 0.5 M HCl was added to liberate the ligand-derived products. The ¹H NMR spectrum of the organic products lacks resonances due to diphenic anhydride. Indeed, GC indicated that phenanthrenequinone was produced in 14% yield along with a negligible amount of diphenic anhydride (ca. 0.5% yield; Figure S23).

The lack of intradiol cleaving reactivity of [PhTt^{tBu}]Ni(phenSQ) contrasts with the reactivity displayed by [PhTt^{tBu}]Fe(phenSQ), highlighting the crucial role of the metal ion in effecting the intradiol cleavage. The general intradiol cleavage mechanism invokes the formation of a metal(III) alkylperoxo intermediate.^{26,76,77} Because the redox potential for the nickel(III)/nickel(II) couple is much higher than that for the iron(III)/iron(II) couple, a nickel(III) alkylperoxo intermediate would not form as readily as an iron(III) alkylperoxo intermediate. Therefore, in the case of [PhTt^{tBu}]Ni(phenSQ), the rate of electron transfer from the phenSQ ligand to O₂ outcompetes the rate of formation of the nickel(III) alkylperoxo intermediate. As a result, phenanthrenequinone was formed rather than diphenic anhydride.

In contrast to its phenSQ counterpart, [PhTt^{tBu}]Ni(3,5-DBSQ) is inert toward O₂. No spectral change was observed after stirring of a toluene solution of [PhTt^{tBu}]Ni(3,5-DBSQ) under an O₂ atmosphere for 12 h (Figure S19). The results of the O₂ reactivity studies on [PhTt^{tBu}]Ni(phenSQ) and

[PhTt^{tBu}]Ni(3,5-DBSQ) are summarized in Scheme 4. The difference in the O₂ reactivity between [PhTt^{tBu}]Ni(phenSQ) and

Scheme 4. O₂ Reactivity of [PhTt^{tBu}]Ni(phenSQ) and [PhTt^{tBu}]Ni(3,5-DBSQ)



and [PhTt^{tBu}]Ni(3,5-DBSQ) implies that the dioxolene ligand also plays an important role in affecting the O₂ reactivity, which was further interrogated through electrochemical studies (vide infra).

3.6. Redox Properties of [PhTt^{tBu}]Fe(phenSQ), [PhTt^{tBu}]Ni(phenSQ), and [PhTt^{tBu}]Ni(3,5-DBSQ). The redox properties of [PhTt^{tBu}]Fe(phenSQ), [PhTt^{tBu}]Ni(phenSQ), and [PhTt^{tBu}]Ni(3,5-DBSQ) were probed using CV and DPV. The cyclic voltammograms of the three complexes are shown in Figure 13. The CV of [PhTt^{tBu}]Fe-

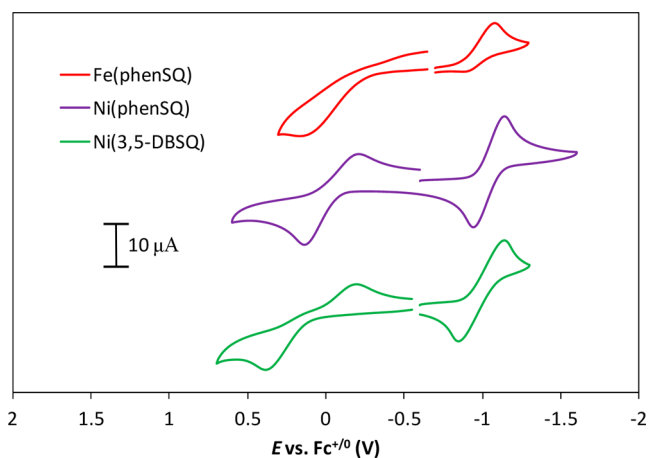


Figure 13. Cyclic voltammograms of 1.0 mM solutions of [PhTt^{tBu}]Fe(phenSQ), [PhTt^{tBu}]Ni(phenSQ), and [PhTt^{tBu}]Ni(3,5-DBSQ) in THF containing 0.1 M *n*-Bu₄NClO₄ under an atmosphere of N₂ (scan rate: 100 mV/s).

(phenSQ) shows irreversible oxidation and reduction events. Interestingly, while the oxidation process is irreversible at scan rates up to 1 V/s, detection of the anodic current associated with the reduction couple is only observed at faster scan rates, which suggests strongly that the one-electron reduction product of [PhTt^{tBu}]Fe(phenSQ) is also relatively unstable (Figure S25). By contrast, the cyclic voltammogram of [PhTt^{tBu}]Ni(phenSQ) exhibits quasi-reversible oxidation and reversible reduction processes, suggesting that the kinetic stability of the oxidation and reduction products of [PhTt^{tBu}]Ni(phenSQ) is much greater than that of [PhTt^{tBu}]Fe(phenSQ). [PhTt^{tBu}]Ni(3,5-DBSQ) exhibits a reversible reduction and an irreversible oxidation wave, indicating that on the time scale of the voltammetry experiments the one-electron-oxidation product of

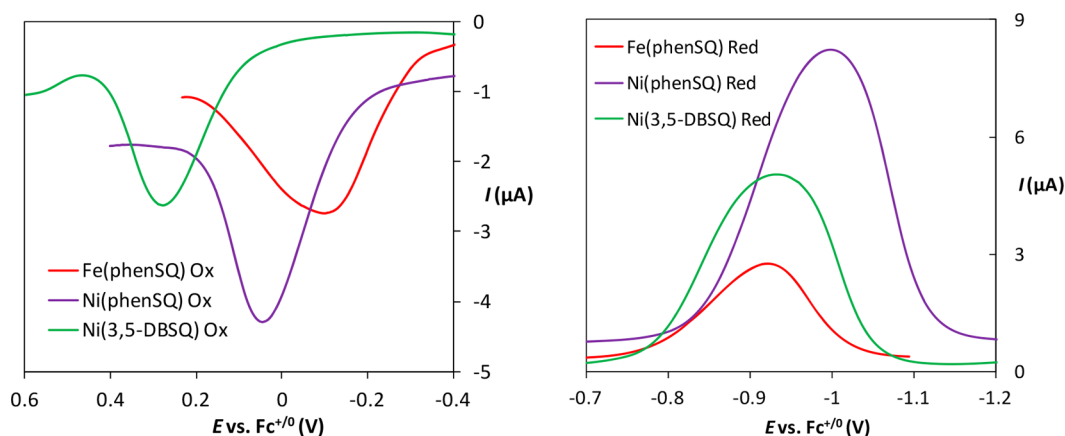


Figure 14. Differential pulse voltammograms of $[\text{PhTt}^{\text{tBu}}]\text{Fe}(\text{phenSQ})$, $[\text{PhTt}^{\text{tBu}}]\text{Ni}(\text{phenSQ})$, and $[\text{PhTt}^{\text{tBu}}]\text{Ni}(3,5\text{-DBSQ})$ in THF (1.0 mM) containing 0.1 M $n\text{-Bu}_4\text{NClO}_4$. Left: oxidation side. Right: reduction side. Experimental parameters: 0.004 V potential increment, 0.05 V pulse amplitude, 0.05 s pulse width, 0.0167 s sampling width, and 0.5 s pulse period.

$[\text{PhTt}^{\text{tBu}}]\text{Ni}(3,5\text{-DBSQ})$ is less stable than the one-electron-oxidation product of $[\text{PhTt}^{\text{tBu}}]\text{Ni}(\text{phenSQ})$.

To garner information regarding the redox potentials at thermodynamic equilibrium for the irreversible redox events, differential pulse voltammograms were collected (Figure 14). Oxidation of $[\text{PhTt}^{\text{tBu}}]\text{Fe}(\text{phenSQ})$ and $[\text{PhTt}^{\text{tBu}}]\text{Ni}(\text{phenSQ})$ was observed at -0.10 and 0.05 V (vs Fc^+/Fc^0), respectively. These redox events are attributed to ligand-based phenSQ/phenQ redox cycling, which occur at similar potentials for other $\text{M}^{\text{II}}(\text{phenSQ})$ complexes.^{78,79} The higher potential of the phenSQ/phenQ couple for $[\text{PhTt}^{\text{tBu}}]\text{Ni}(\text{phenSQ})$, compared to that for $[\text{PhTt}^{\text{tBu}}]\text{Fe}(\text{phenSQ})$, can be attributed to (a) a greater LF stabilization energy (LFSE) for high-spin Ni^{II} d^8 versus high-spin Fe^{II} d^6 and (b) a stronger antiferromagnetic exchange in $[\text{PhTt}^{\text{tBu}}]\text{Ni}(\text{phenSQ})$. A similar trend was observed by Pierpont et al. in their studies of the $[\text{Tp}^{\text{Cum,Me}}]\text{M}(3,5\text{-DBSQ})$ series ($\text{M} = \text{Zn}^{\text{II}}$, Cu^{II} , and Co^{II}).⁸⁰ In their case, the zinc(II) analogue, which has no LFSE and no exchange interaction between the diamagnetic Zn^{II} ion and the semiquinonate radical, has an oxidation potential that is 0.15 and 0.17 V lower than those of the copper(II) and cobalt(II) analogues, respectively. The oxidation of $[\text{PhTt}^{\text{tBu}}]\text{Ni}(3,5\text{-DBSQ})$ to $[\text{PhTt}^{\text{tBu}}]\text{Ni}(3,5\text{-DBQ})^+$ occurs at 0.28 V, which is 0.23 V higher than the potential at which $[\text{PhTt}^{\text{tBu}}]\text{Ni}(\text{phenSQ})$ is oxidized to $[\text{PhTt}^{\text{tBu}}]\text{Ni}(\text{phenQ})^+$. These data indicate that $[\text{PhTt}^{\text{tBu}}]\text{Ni}(3,5\text{-DBSQ})$ is more resistant toward oxidation of the semiquinonate ligand than $[\text{PhTt}^{\text{tBu}}]\text{Ni}(\text{phenSQ})$, which provides an explanation for why $[\text{PhTt}^{\text{tBu}}]\text{Ni}(3,5\text{-DBSQ})$ does not react with O_2 , whereas $[\text{PhTt}^{\text{tBu}}]\text{Ni}(\text{phenSQ})$ does.

The oxidation potentials of $[\text{PhTt}^{\text{tBu}}]\text{Fe}(\text{phenSQ})$ and $[\text{PhTt}^{\text{tBu}}]\text{Ni}(\text{phenSQ})$ also provide clues as to whether the oxidation product phenQ is generated through an outer-sphere or inner-sphere electron-transfer mechanism. The redox potential of O_2/O_2^- is around -1.0 V versus SCE (ca. -1.5 V vs Fc^+/Fc^0),⁸¹ which is much lower than the redox potential of phenSQ/phenQ. Thus, direct electron transfer from phenSQ to O_2 is unlikely. Instead, phenQ may be generated through an inner-sphere electron-transfer mechanism, which involves binding of O_2 to the metal, followed by electron transfer from the phenSQ ligand to the $\text{M}(\text{O}_2)$ moiety. Under this mechanism, the low O_2 affinity of nickel(II) disfavors the O_2 binding and, therefore, makes the formation of phenQ sluggish.

On the reduction side of the differential pulse voltammograms, $[\text{PhTt}^{\text{tBu}}]\text{Fe}(\text{phenSQ})$ and $[\text{PhTt}^{\text{tBu}}]\text{Ni}(\text{phenSQ})$ are reduced at -0.92 and -1.00 V, respectively. These events are assigned as the phenSQ/phenCat redox couple. The reduction of $[\text{PhTt}^{\text{tBu}}]\text{Ni}(3,5\text{-DBSQ})$ at -0.94 V is assigned to a 3,5-DBSQ/3,5-DBCat redox couple. A comparison of the reduction potentials of $[\text{PhTt}^{\text{tBu}}]\text{Ni}(3,5\text{-DBSQ})$ and $[\text{PhTt}^{\text{tBu}}]\text{Ni}(\text{phenSQ})$ reveals that it is easier to reduce 3,5-DBSQ to its catecholate form, which explains the inability to isolate an iron(II) semiquinonate complex with 3,5-DBSQ as the ligand.

4. CONCLUSIONS

The geometric and electronic structures of a previously reported iron(II) *o*-semiquinonate complex, $[\text{PhTt}^{\text{tBu}}]\text{Fe}(\text{phenSQ})$,³⁶ and two new nickel(II) *o*-semiquinonate complexes, $[\text{PhTt}^{\text{tBu}}]\text{Ni}(\text{phenSQ})$ and $[\text{PhTt}^{\text{tBu}}]\text{Ni}(3,5\text{-DBSQ})$, were elucidated by X-ray crystallography, optical and NMR spectroscopies, SQUID magnetometry, and DFT calculations. All three complexes contain high-spin M^{II} ions antiferromagnetically coupled to the semiquinonate radicals, with $[\text{PhTt}^{\text{tBu}}]\text{Ni}(3,5\text{-DBSQ})$ having the largest exchange interaction ($J = -382$ cm^{-1}), followed by $[\text{PhTt}^{\text{tBu}}]\text{Ni}(\text{phenSQ})$ ($J = -320$ cm^{-1}) and then $[\text{PhTt}^{\text{tBu}}]\text{Fe}(\text{phenSQ})$ ($J = -127$ cm^{-1}). The trend of the magnitude of exchange interactions between the M^{II} ions and the semiquinonate ligands is well reproduced by the DFT calculations.

The fact that $[\text{PhTt}^{\text{tBu}}]\text{Fe}(\text{phenSQ})$ exhibits intradiol cleaving reactivity provides new evidence supporting the theory that the iron(II) semiquinonate character within the iron(III) catecholate species could be responsible for the O_2 reactivity of intradiol catechol dioxygenases. The O_2 reactivity studies further reveal the importance of the metal ion on the intradiol cleaving reactivity because changing the metal ion from Fe^{II} to Ni^{II} abolishes the intradiol reactivity and makes the oxidation of phenSQ to phenQ more pronounced. The metal-ion effect is caused by the difference in the redox potentials of the metal(III)/metal(II) couples and, likely, differences in the O_2 binding affinity. When the metal(III)/metal(II) potential is high, as in the case of $[\text{PhTt}^{\text{tBu}}]\text{Ni}(\text{phenSQ})$, the Ni^{II} ion acts as a mediator for the inner-sphere electron transfer from phenSQ to O_2 , generating phenQ. On the other hand, when the midpoint potential of the metal(III)/metal(II) couple is sufficiently low, the formation of the metal(III) alkylperoxo intermediate outcompetes the inner-sphere electron transfer

and, thus, the reaction produces primarily the intradiol cleavage product. Last, the lack of any O₂ reactivity of [PhTt^{tBu}]Ni(3,5-DBSQ) indicates that the midpoint potential of the semi-quinone/quinone couple also affects the outcome of the O₂ reactions. This assertion is further supported by the results of the electrochemical studies, which show that the midpoint potential for the 3,5-DBSQ/DBQ couple is higher than that of the phenSQ/phenQ couple.

■ ASSOCIATED CONTENT

📄 Supporting Information

The Supporting Information is available free of charge on the ACS Publications website at DOI: 10.1021/acs.inorgchem.7b01491.

¹H NMR and LIFDI-MS spectra, magnetization data, calculated EDDMs, TD-DFT-calculated absorption spectra for models Fe(phenSQ)₂, Ni(phenSQ)₂, and Ni(3,5-DBSQ)₂, experimental TD-DFT-calculated absorption spectra, MO diagram for model Ni(3,5-DBSQ)₃, GC data, and CV scan rate data for [PhTt^{tBu}]Fe(phenSQ) (PDF)

Accession Codes

CCDC 1541366–1541368 contain the supplementary crystallographic data for this paper. These data can be obtained free of charge via www.ccdc.cam.ac.uk/data_request/cif, or by emailing data_request@ccdc.cam.ac.uk, or by contacting The Cambridge Crystallographic Data Centre, 12 Union Road, Cambridge CB2 1EZ, UK; fax: +44 1223 336033.

■ AUTHOR INFORMATION

Corresponding Author

*E-mail: riordan@udel.edu

ORCID

Thomas C. Brunold: 0000-0001-6516-598X

Charles G. Riordan: 0000-0002-8572-4571

Notes

The authors declare no competing financial interest.

■ ACKNOWLEDGMENTS

C.G.R. acknowledges financial support of the National Science Foundation (NSF) through Award CHE-1112035. C.V.P. acknowledges support from the NSF through Award CHE-1445959. M.M.K. acknowledges financial support through an NSF graduate fellowship. K.R.D. gratefully acknowledges the Robert A. Welch Foundation (A-1449) for financial support.

■ REFERENCES

- (1) Pierpont, C. G.; Buchanan, R. M. Transition metal complexes of *o*-benzoquinone, *o*-semiquinone, and catecholate ligands. *Coord. Chem. Rev.* **1981**, *38*, 45–87.
- (2) Pierpont, C. G. Studies on charge distribution and valence tautomerism in transition metal complexes of catecholate and semiquinone ligands. *Coord. Chem. Rev.* **2001**, *216–217*, 99–125.
- (3) Hendrickson, D. N.; Pierpont, C. G. Valence Tautomeric Transition Metal Complexes. *Top. Curr. Chem.* **2004**, *234*, 63–95.
- (4) Tezgerevska, T.; Alley, K. G.; Boskovic, C. Valence tautomerism in metal complexes: Stimulated and reversible intramolecular electron transfer between metal centers and organic ligands. *Coord. Chem. Rev.* **2014**, *268*, 23–40.
- (5) Sato, O.; Tao, J.; Zhang, Y. Z. Control of magnetic properties through external stimuli. *Angew. Chem., Int. Ed.* **2007**, *46*, 2152–2187.

(6) Sato, O.; Cui, A.; Matsuda, R.; Tao, J.; Hayami, S. Photo-induced Valence Tautomerism in Co Complexes. *Acc. Chem. Res.* **2007**, *40*, 361–369.

(7) Dei, A.; Gatteschi, D.; Sangregorio, C.; Sorace, L. Quinonoid Metal Complexes: Toward Molecular Switches. *Acc. Chem. Res.* **2004**, *37*, 827–835.

(8) Tichnell, C. R.; Shultz, D. A.; Popescu, C. V.; Sokirniy, I.; Boyle, P. D. Synthesis, Characterization, and Photophysical Studies of an Iron(III) Catecholate-Nitronylnitroxide Spin-Crossover Complex. *Inorg. Chem.* **2015**, *54*, 4466–4474.

(9) Girerd, J. J.; Boillot, M. L.; Blain, G.; Rivière, E. An EPR investigation of the electronic structure of pseudo-octahedral and spin crossover catecholato-iron(III) complexes in the low-spin state. *Inorg. Chim. Acta* **2008**, *361*, 4012–4016.

(10) Simaan, A. J.; Boillot, M. L.; Carrasco, R.; Cano, J.; Girerd, J. J.; Mattioli, T. A.; Ensling, J.; Spiering, H.; Gülich, P. Electronic, vibrational, and structural properties of a spin-crossover catecholato-iron system in the solid state: theoretical study of the electronic nature of the doublet and sextet states. *Chem. - Eur. J.* **2005**, *11*, 1779–1793.

(11) Floquet, S.; Simaan, A. J.; Rivière, E.; Nierlich, M.; Thuéry, P.; Ensling, J.; Gülich, P.; Girerd, J. J.; Boillot, M. L. Spin crossover of ferric complexes with catecholate derivatives. Single-crystal X-ray structure, magnetic and Mossbauer investigations. *Dalton Trans.* **2005**, 1734–1742.

(12) Simaan, A. J.; Boillot, M.-L.; Rivière, E.; Boussac, A.; Girerd, J.-J. A Two-Step Spin Crossover in [(TPA)Fe^{III}(cat)]BPh₄. *Angew. Chem., Int. Ed.* **2000**, *39*, 196–198.

(13) Graf, M.; Wolmershauser, G.; Kelm, H.; Demeschko, S.; Meyer, F.; Krüger, H. J. Temperature-induced spin-transition in a low-spin cobalt(II) semiquinone complex. *Angew. Chem., Int. Ed.* **2010**, *49*, 950–953.

(14) Rupp, F.; Chevalier, K.; Graf, M.; Schmitz, M.; Kelm, H.; Grün, A.; Zimmer, M.; Gerhards, M.; van Wüllen, C.; Krüger, H.-J.; Diller, R. Spectroscopic, Structural, and Kinetic Investigation of the Ultrafast Spin Crossover in an Unusual Cobalt(II) Semiquinone Radical Complex. *Chem. - Eur. J.* **2017**, *23*, 2119–2132.

(15) Bugg, T. D. H. Dioxygenase enzymes: catalytic mechanisms and chemical models. *Tetrahedron* **2003**, *59*, 7075–7101.

(16) Costas, M.; Mehn, M. P.; Jensen, M. P.; Que, L., Jr. Dioxygen Activation at Mononuclear Nonheme Iron Active Sites: Enzymes, Models, and Intermediates. *Chem. Rev.* **2004**, *104*, 939–986.

(17) Palaniandavar, M.; Mayilmurugan, R. Mononuclear non-heme iron(III) complexes as functional models for catechol dioxygenases. *C. R. Chim.* **2007**, *10*, 366–379.

(18) Dey, S. K.; Mukherjee, A. Catechol oxidase and phenoxazinone synthase: Biomimetic functional models and mechanistic studies. *Coord. Chem. Rev.* **2016**, *310*, 80–115.

(19) Jastrzebski, R.; Weckhuysen, B. M.; Bruijninx, P. C. Catalytic oxidative cleavage of catechol by a non-heme iron(III) complex as a green route to dimethyl adipate. *Chem. Commun.* **2013**, *49*, 6912–6914.

(20) Chatterjee, S.; Sheet, D.; Paine, T. K. Catalytic and regiospecific extradiol cleavage of catechol by a biomimetic iron complex. *Chem. Commun.* **2013**, *49*, 10251–10253.

(21) Koch, W. O.; Krüger, H.-J. A Highly Reactive and Catalytically Active Model System for Intradiol-Cleaving Catechol Dioxygenases: Structure and Reactivity of Iron(III) Catecholate Complexes of *N,N'*-Dimethyl-2,11-diaza[3.3](2,6)pyridinophane. *Angew. Chem., Int. Ed. Engl.* **1996**, *34*, 2671–2674.

(22) Ikeda, A.; Hoshino, K.; Komatsuzaki, H.; Satoh, M.; Nakazawa, J.; Hikichi, S. O₂ activation and external substrate oxidation capability of a Co(II)–semiquinonate complex. *New J. Chem.* **2013**, *37*, 2377–2383.

(23) Hitomi, Y.; Ando, A.; Matsui, H.; Ito, T.; Tanaka, T.; Ogo, S.; Funabiki, T. Aerobic Catechol Oxidation Catalyzed by a Bis(μ-oxo)dimanganese(III,III) Complex via a Manganese(II)–Semiquinonate Complex. *Inorg. Chem.* **2005**, *44*, 3473–3478.

- (24) Rolle, C. J., III; Hardcastle, K. I.; Soper, J. D. Reactions of Tetrabromocatecholatomanganese(III) Complexes with Dioxygen. *Inorg. Chem.* **2008**, *47*, 1892–1894.
- (25) Bugg, T. D.; Ramaswamy, S. Non-heme iron-dependent dioxygenases: unravelling catalytic mechanisms for complex enzymatic oxidations. *Curr. Opin. Chem. Biol.* **2008**, *12*, 134–140.
- (26) Knoot, C. J.; Purpero, V. M.; Lipscomb, J. D. Crystal structures of alkylperoxy and anhydride intermediates in an intradiol ring-cleaving dioxygenase. *Proc. Natl. Acad. Sci. U. S. A.* **2015**, *112*, 388–393.
- (27) Funabiki, T.; Yamazaki, T. Mechanism of oxygenative cleavage of catechols by nonheme iron complexes in relevance to catechol dioxygenases studied by quantum chemical calculations. *J. Mol. Catal. A: Chem.* **1999**, *150*, 37–47.
- (28) Nakatani, N.; Hitomi, Y.; Sakaki, S. Multistate CASPT2 study of native iron(III)-dependent catechol dioxygenase and its functional models: electronic structure and ligand-to-metal charge-transfer excitation. *J. Phys. Chem. B* **2011**, *115*, 4781–4789.
- (29) Borowski, T.; Siegbahn, P. E. M. Mechanism for Catechol Ring Cleavage by Non-Heme Iron Intradiol Dioxygenases: A Hybrid DFT Study. *J. Am. Chem. Soc.* **2006**, *128*, 12941–12953.
- (30) Georgiev, V.; Noack, H.; Borowski, T.; Blomberg, M. R. A.; Siegbahn, P. E. M. DFT Study on the Catalytic Reactivity of a Functional Model Complex for Intradiol-Cleaving Dioxygenases. *J. Phys. Chem. B* **2010**, *114*, 5878–5885.
- (31) Cox, D. D.; Que, L., Jr. Functional Models for Catechol 1,2-Dioxygenase. The Role of the Iron(III) Center. *J. Am. Chem. Soc.* **1988**, *110*, 8085–8092.
- (32) Jang, H. G.; Cox, D. D.; Que, L., Jr. A Highly Reactive Functional Model for the Catechol Dioxygenases. Structure and Properties of [Fe(TPA)DBC]BPh₄. *J. Am. Chem. Soc.* **1991**, *113*, 9200–9204.
- (33) Duda, M.; Pascaly, M.; Krebs, B. A highly reactive functional model for catechol 1,2-dioxygenase: reactivity studies of iron(III) catecholate complexes of bis[(2-pyridyl)methyl][(1-methylimidazol-2-yl)methyl]amine. *Chem. Commun.* **1997**, 835–836.
- (34) Funabiki, T.; Fukui, A.; Hitomi, Y.; Higuchi, M.; Yamamoto, T.; Tanaka, T.; Tani, F.; Naruta, Y. Structures and electronic properties of the catecholatoiron complexes in relation to catechol dioxygenases: chlorocatecholatoiron complexes are compared to the 3,5-di-tert-butylcatecholatoiron complex in the solid state and in solution. *J. Inorg. Biochem.* **2002**, *91*, 151–158.
- (35) Hitomi, Y.; Yoshida, M.; Higuchi, M.; Minami, H.; Tanaka, T.; Funabiki, T. A linear correlation between energy of LMCT band and oxygenation reaction rate of a series of catecholatoiron(III) complexes: initial oxygen binding during intradiol catechol oxygenation. *J. Inorg. Biochem.* **2005**, *99*, 755–763.
- (36) Wang, P.; Yap, G. P. A.; Riordan, C. G. Five-coordinate M^{II}-semiquinonate (M = Fe, Mn, Co) complexes: reactivity models of the catechol dioxygenases. *Chem. Commun.* **2014**, *50*, 5871–5873.
- (37) Schebler, P. J.; Riordan, C. G.; Guzei, I. A.; Rheingold, A. L. Phenyltris((tert-butylthio)methyl)borate: A Second Generation S₃⁻ Ligand That Enforces Tetrahedral Coordination. *Inorg. Chem.* **1998**, *37*, 4754–4755.
- (38) Muraev, V. A.; Abakumov, G. A.; Razuvaev, G. A. ESR-Spectra of Ortho-semiquinolates of Univalent Thallium. *Dokl. Akad. Nauk SSSR* **1974**, *217*, 1083–1086.
- (39) Evans, D. F. The determination of the paramagnetic susceptibility of substances in solution by nuclear magnetic resonance. *J. Chem. Soc.* **1959**, 2003–2005.
- (40) Live, D. H.; Chan, S. I. Bulk susceptibility corrections in nuclear magnetic resonance experiments using superconducting solenoids. *Anal. Chem.* **1970**, *42*, 791–792.
- (41) Bain, G. A.; Berry, J. F. Diamagnetic Corrections and Pascal's Constants. *J. Chem. Educ.* **2008**, *85*, 532–536.
- (42) Linden, H. Liquid injection field desorption ionization: a new tool for soft ionization of samples including air sensitive catalysts and non-polar hydrocarbons. *Eur. Mass Spectrom.* **2004**, *10*, 459–468.
- (43) Gross, J. H.; Nieth, N.; Linden, H. B.; Blumbach, U.; Richter, F. J.; Tauchert, M. E.; Tompers, R.; Hofmann, P. Liquid injection field desorption/ionization of reactive transition metal complexes. *Anal. Bioanal. Chem.* **2006**, *386*, 52–58.
- (44) Noviandri, I.; Brown, K. N.; Fleming, D. S.; Gulyas, P. T.; Lay, P. A.; Masters, A. F.; Phillips, L. The Decamethylferrocenium/Decamethylferrocene Redox Couple: A Superior Redox Standard to the Ferrocenium/Ferrocene Redox Couple for Studying Solvent Effects on the Thermodynamics of Electron Transfer. *J. Phys. Chem. B* **1999**, *103*, 6713–6722.
- (45) Sheldrick, G. Crystal structure refinement with SHELXL. *Acta Crystallogr., Sect. C: Struct. Chem.* **2015**, *71*, 3–8.
- (46) Neese, F. ORCA: An *ab initio*, DFT and semiempirical SCF-MO package, version 2.9.0; Information Technology Services, The University of Hong Kong, 2012.
- (47) Schäfer, A.; Huber, C.; Ahlrichs, R. Fully optimized contracted Gaussian basis sets of triple zeta valence quality for atoms Li to Kr. *J. Chem. Phys.* **1994**, *100*, 5829–5835.
- (48) Schäfer, A.; Horn, H.; Ahlrichs, R. Fully optimized contracted Gaussian basis sets for atoms Li to Kr. *J. Chem. Phys.* **1992**, *97*, 2571–2577.
- (49) Becke, A. D. Density-functional thermochemistry. III. The role of exact exchange. *J. Chem. Phys.* **1993**, *98*, 5648–5652.
- (50) Lee, C. T.; Yang, W. T.; Parr, R. G. Development of the Colle-Salvetti correlation-energy formula into a functional of the electron density. *Phys. Rev. B: Condens. Matter Mater. Phys.* **1988**, *37*, 785–789.
- (51) Becke, A. D. Density-functional exchange-energy approximation with correct asymptotic behavior. *Phys. Rev. A: At., Mol., Opt. Phys.* **1988**, *38*, 3098–3100.
- (52) Perdew, J. P. BP86. *Phys. Rev. B: Condens. Matter Mater. Phys.* **1986**, *33*, 8822–8824.
- (53) Perdew, J. P. BP86 correction. *Phys. Rev. B: Condens. Matter Mater. Phys.* **1986**, *34*, 7406–7406.
- (54) Romelt, M.; Ye, S.; Neese, F. Calibration of Modern Density Functional Theory Methods for the Prediction of Fe-57 Mossbauer Isomer Shifts: Meta-GGA and Double-Hybrid Functionals. *Inorg. Chem.* **2009**, *48*, 784–785.
- (55) Mock, M. T.; Popescu, C. V.; Yap, G. P. A.; Dougherty, W. G.; Riordan, C. G. Monovalent Iron in a Sulfur-Rich Environment. *Inorg. Chem.* **2008**, *47*, 1889–1891.
- (56) Bittner, M. M.; Lindeman, S. V.; Popescu, C. V.; Fiedler, A. T. Dioxygen reactivity of biomimetic Fe(II) complexes with noninnocent catecholate, o-aminophenolate, and o-phenylenediamine ligands. *Inorg. Chem.* **2014**, *53*, 4047–4061.
- (57) Baum, A. E.; Park, H.; Lindeman, S. V.; Fiedler, A. T. Synthesis and spectroscopic characterization of high-spin mononuclear iron(II) *p*-semiquinonate complexes. *Inorg. Chem.* **2014**, *53*, 12240–12242.
- (58) Baum, A. E.; Lindeman, S. V.; Fiedler, A. T. Mononuclear Iron-(hydro/semi)quinonate Complexes Featuring Neutral and Charged Scorpionates: Synthetic Models of Intermediates in the Hydroquinone Dioxygenase Mechanism. *Eur. J. Inorg. Chem.* **2016**, *2016*, 2455–2464.
- (59) Chilton, N. F.; Anderson, R. P.; Turner, L. D.; Soncini, A.; Murray, K. S. PHI: A powerful new program for the analysis of anisotropic monomeric and exchange-coupled polynuclear d- and f-block complexes. *J. Comput. Chem.* **2013**, *34*, 1164–1175.
- (60) Mayilmurugan, R.; Visvaganesan, K.; Suresh, E.; Palaniandavar, M. Iron(III) complexes of tripodal monophenolate ligands as models for non-heme catechol dioxygenase enzymes: correlation of dioxygenase activity with ligand stereoelectronic properties. *Inorg. Chem.* **2009**, *48*, 8771–8783.
- (61) Balamurugan, M.; Vadivelu, P.; Palaniandavar, M. Iron(III) complexes of tripodal tetradentate 4N ligands as functional models for catechol dioxygenases: the electronic vs. steric effect on extradiol cleavage. *Dalton Trans.* **2014**, *43*, 14653–14668.
- (62) Váradi, T.; Pap, J. S.; Giorgi, M.; Párkányi, L.; Csay, T.; Speier, G.; Kaizer, J. Iron(III) complexes with meridional ligands as functional models of intradiol-cleaving catechol dioxygenases. *Inorg. Chem.* **2013**, *52*, 1559–1569.

(63) Panda, M. K.; John, A.; Shaikh, M. M.; Ghosh, P. Mimicking the Intradiol Catechol Cleavage Activity of Catechol Dioxygenase by High-Spin Iron(III) Complexes of a New Class of a Facially Bound [N₂O] Ligand. *Inorg. Chem.* **2008**, *47*, 11847–11856.

(64) Bruijninx, P. C. A.; Lutz, M.; Spek, A. L.; Hagen, W. R.; van Koten, G.; Klein Gebbink, R. J. M. Iron(III)–Catecholates Complexes as Structural and Functional Models of the Intradiol-Cleaving Catechol Dioxygenases. *Inorg. Chem.* **2007**, *46*, 8391–8402.

(65) Li, F.; Wang, M.; Li, P.; Zhang, T.; Sun, L. Iron(III) Complexes with a Tripodal N₃O Ligand Containing an Internal Base as a Model for Catechol Intradiol-Cleaving Dioxygenases. *Inorg. Chem.* **2007**, *46*, 9364–9371.

(66) Dhanalakshmi, T.; Suresh, E.; Palaniandavar, M. Synthesis, structure, spectra and reactivity of iron(III) complexes of imidazole and pyrazole containing ligands as functional models for catechol dioxygenases. *Dalton Trans.* **2009**, 8317–8328.

(67) Lakshman, T. R.; Chatterjee, S.; Chakraborty, B.; Paine, T. K. Substrate-dependent aromatic ring fission of catechol and 2-aminophenol with O₂ catalyzed by a nonheme iron complex of a tripodal N₄ ligand. *Dalton Trans.* **2016**, *45*, 8835–8844.

(68) Farrell, J. R.; Niconchuk, J. A.; Renahan, P. R.; Higham, C. S.; Yoon, E.; Andrews, M. V.; Shaw, J. L.; Cetin, A.; Engle, J.; Ziegler, C. J. New diamino-diheterophenol ligands coordinate iron(III) to make structural and functional models of protocatechuate 3,4-dioxygenase. *Dalton Trans.* **2014**, *43*, 6610–6613.

(69) Addison, A. W.; Rao, T. N.; Reedijk, J.; van Rijn, J.; Verschoor, G. C. Synthesis, structure, and spectroscopic properties of copper(II) compounds containing nitrogen–sulphur donor ligands; the crystal and molecular structure of aqua[1,7-bis(N-methylbenzimidazol-2'-yl)-2,6-dithiaheptane]copper(II) perchlorate. *J. Chem. Soc., Dalton Trans.* **1984**, 1349–1356.

(70) Shultz, D. A.; Vostrikova, K. E.; Bodnar, S. H.; Koo, H.-J.; Whangbo, M.-H.; Kirk, M. L.; Depperman, E. C.; Kampf, J. W. Trends in Metal–Biradical Exchange Interaction for First-Row M^{II}(Nitronyl Nitroxide–Semiquinone) Complexes. *J. Am. Chem. Soc.* **2003**, *125*, 1607–1617.

(71) Cho, J.; Yap, G. P. A.; Riordan, C. G. Structural, Spectroscopic, and Electrochemical Properties of a Series of High-Spin Thiolatonicel(II) Complexes. *Inorg. Chem.* **2007**, *46*, 11308–11315.

(72) Fujita, K.; Schenker, R.; Gu, W.; Brunold, T. C.; Cramer, S. P.; Riordan, C. G. A Monomeric Nickel–Dioxygen Adduct Derived from a Nickel(I) Complex and O₂. *Inorg. Chem.* **2004**, *43*, 3324–3326.

(73) Benelli, C.; Dei, A.; Gatteschi, D.; Pardi, L. Electronic Structure and Reactivity of Dioxolene Adducts of Nickel(II) and Copper(II) Triazamacrocyclic Complexes. *Inorg. Chem.* **1990**, *29*, 3409–3415.

(74) Kieber-Emmons, M. T.; Annaraj, J.; Seo, M. S.; Van Heuvelen, K. M.; Tosha, T.; Kitagawa, T.; Brunold, T. C.; Nam, W.; Riordan, C. G. Identification of an “End-on” Nickel–Superoxo Adduct, [Ni(tmc)-(O₂)]⁺. *J. Am. Chem. Soc.* **2006**, *128*, 14230–14231.

(75) Kieber-Emmons, M. T.; Riordan, C. G. Dioxygen Activation at Monovalent Nickel. *Acc. Chem. Res.* **2007**, *40*, 618–625.

(76) Pau, M. Y. M.; Davis, M. I.; Orville, A. M.; Lipscomb, J. D.; Solomon, E. I. Spectroscopic and Electronic Structure Study of the Enzyme–Substrate Complex of Intradiol Dioxygenases: Substrate Activation by a High-Spin Ferric Non-heme Iron Site. *J. Am. Chem. Soc.* **2007**, *129*, 1944–1958.

(77) Jastrzebski, R.; Quesne, M. G.; Weckhuysen, B. M.; de Visser, S. P.; Bruijninx, P. C. A. Experimental and Computational Evidence for the Mechanism of Intradiol Catechol Dioxygenation by Non-Heme Iron(III) Complexes. *Chem. - Eur. J.* **2014**, *20*, 15686–15691.

(78) Caneschi, A.; Dei, A.; Gatteschi, D.; Tangoulis, V. Antiferromagnetic Coupling in a Six-Coordinate High Spin Cobalt(II)–Semiquinonato Complex. *Inorg. Chem.* **2002**, *41*, 3508–3512.

(79) Bencini, A.; Carbonera, C.; Dei, A.; Vaz, M. G. F. Magnetic exchange interaction between paramagnetic transition metal ions and radical ligands. A 9,10-dioxophenanthrenesemiquinonato adduct of a nickel(II)–tetraazamacrocyclic complex and DFT description. *Dalton Trans.* **2003**, 1701–1706.

(80) Ruf, M.; Noll, B. C.; Groner, M. D.; Yee, G. T.; Pierpont, C. G. Pocket Semiquinone Complexes of Cobalt(II), Copper(II), and Zinc(II) Prepared with the Hydrotris(cumenylmethylpyrazolyl)borate Ligand. *Inorg. Chem.* **1997**, *36*, 4860–4865.

(81) AlNashef, I. M.; Leonard, M. L.; Kittle, M. C.; Matthews, M. A.; Weidner, J. W. Electrochemical Generation of Superoxide in Room-Temperature Ionic Liquids. *Electrochem. Solid-State Lett.* **2001**, *4*, D16–D18.